Journal of Materials Chemistry C

Accepted Manuscript

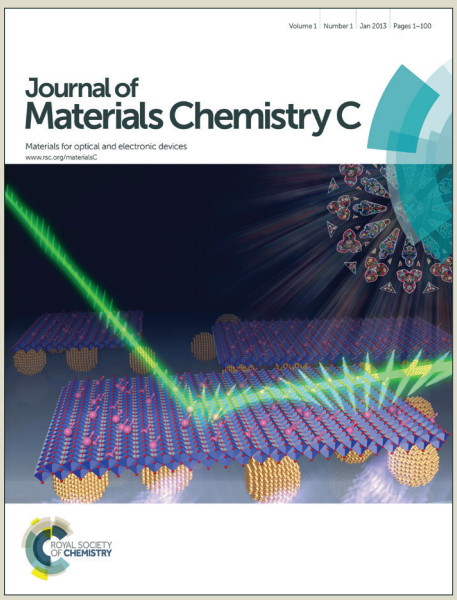

ROYAL SOCIETY OF CHEMISTRY

www.rsc.org/materialsC

Electronic Properties of Nano-Structured Bismuth-Antimony Materials

Shuang Tang*[1], Mildred S. Dresselhaus†[2,3]

[1]Department of Materials Science and Engineering, Massachusetts Institute of Technology, Cambridge, MA, 02139-4037, USA; *tangs@mit.edu

[2]Department of Electrical Engineering and Computer Science, Massachusetts Institute of Technology Cambridge, MA, 02139-4037, USA; †millie@mgm.mit.edu

[3]Department of Physics, Massachusetts Institute of Technology Cambridge, MA, 02139-4037, USA;

Abstract

Bismuth antimony ($Bi_{1-x}Sb_x$) is one of the most important materials system for fundamental materials science, condensed matter physics, low temperature thermoelectrics, infrared applications, and beyond. The bulk materials have been studied for many decades. Recently, nanoscience and nanotechnology has been introduced to this materials system, which has brought much more interest and attention for both research and applications. The present article reviews the up-to-date achievements on electronic properties of nanostructured $Bi_{1-x}Sb_x$, and points out future directions for scientific research in this field.

Author Profiles:

Shuang Tang is now in the Department of Materials Science and Engineering in the Massachusetts Institute of Technology. He is noted for research in bismuth and bismuth antimony related science, Dirac cone science, thermoelectrics, anisotropic transport, nanoscience, from the aspects of materials science and condensed matter physics. Tang established the theory of constructing various types of Dirac cones in 2012, and the theory of pseudo-*ZT*s on thermoelectrics in 2014, with Prof. Mildred Dresselhaus.

Mildred Dresselhaus is the Institute Professor of the Massachusetts Institute of Technology. Dr. Dresselhaus has served as President of the American Physical Society, the American Association for the Advancement of Science, Treasurer of the National Academy of Science, Director of Science of the U. S. Department of Energy, etc. Her honors includes the Kavli Prize, the Enrico Fermi Award, National Medal of Science, etc. She is noted for carbon science, bismuth related science, thermoelectrics, Raman spectroscopy, etc. Her achievements include the Saito-Fujita-Dresselhaus theory on carbon nanotube band structures, the Hicks-Dresselhaus model on low-dimensional thermoelectrics, the Tang-Dresselhaus theory on constructing various anisotropic

Dirac cones, etc.

Introduction

Bismuth antimony ($Bi_{1-x}Sb_x$) materials have been one of the most interesting materials systems for many decades, regarding their highly anisotropic transport properties and small effective mass and high mobility carriers. In the early years, researchers found that the variation of the electronic band structure of bulk $Bi_{1-x}Sb_x$ provided a remarkable richness of electronic properties, when considered as a function of stoichiometry, temperature, strain, pressure, etc. Semimetals, direct band gap semiconducting and indirect band gap semiconducting behaviors have all been observed in this materials class. Furthermore, both parabolically and non-parabollically dispersed charge carriers can be found in this materials class. The high degree of anisotropy in their transport properties also distinguishes the $Bi_{1-x}Sb_x$ materials from other systems. $Bi_{1-x}Sb_x$ alloys are considered to be one of the best materials for low temperature thermoelectrics, infrared devices and millivolt electronics. The electronic transport properties of bulk $Bi_{1-x}Sb_x$ have been studied in great detail.

This materials class has been considered to be one of the best thermoelectric materials for cooling in the low temperature range below 100 K. In the early 1990s, Hicks and Dresselhaus pointed out that nano-structured materials may have enhanced thermoelectric figure of merit compared to their bulk counterparts [1, 2]. Since then, different types of nano-structured $Bi_{1-x}Sb_x$ materials, have notably drawn the attention of researchers, including nanowires [3-7], thin films [8-13], and nano-particles [14-17].

By making these materials in low-dimensional forms, more parameters are introduced to increase the flexibility and controllability of their electronic band structures and therefore, their electronic properties.

Lin et al [3, 18] have theoretically and experimentally shown that the width of $Bi_{1-x}Sb_x$ nanowires can be a useful parameter to enhance Seebeck coefficient. It is easier to add strain to the materials in the $Bi_{1-x}Sb_x$ nanowires system compared to bulk system. Nikolaeva et al [6, 7, 19] et al have found that the strain added to $Bi_{1-x}Sb_x$ nanowires can further control and improve the thermoelectric performance. Rabin et al [4] have proposed the pocket alignment method in $Bi_{1-x}Sb_x$ nanowires system on Seebeck improving, which leads to a theoretical value of *ZT* as high as 2.5.

In 2011, Rogechava et al [10] found that in the mosaic-single-crystal $Bi_{1-x}Sb_x$ films the electrical conductivity and the Seebeck coefficient can be increased at the same time, which is very important for *ZT* enhancement, because the negative correlation between Seebeck coefficient and electrical conductivity in other materials systems is always an obstacle in *ZT* enhancement. Single crystal $Bi_{1-x}Sb_x$ thin films are interesting in topics much beyond thermoelectrics. Tang and Dresselhaus [12, 13] have predicted that different kinds of Dirac cone systems can be synthesized based on the single crystal $Bi_{1-x}Sb_x$ thin films materials, including single-Dirac-cone, bi-Dirac-cone, tri-Dirac-cone, exact-Dirac-cone, semi-Dirac-cone, and quasi-Dirac-cone, and also including Dirac cones with different anisotropic degrees.

In 2007, Fu and Kane predicted the topological insulator phase in $Bi_{1-x}Sb_x$ surface states [20, 21], which is experimentally proved by Hsieh et al [20]. These discover in

$Bi_{1-x}Sb_x$ surface states directly leads to the intensively focused area of topological insulator [22, 23 24, 25], which promises potential applications in spintronics, superconductivity, quantum computing, etc.

Nano-particles/nano-composites system [26] is another promising nano-structure that can enhance thermoelectric *ZT*. So far the reported highest *ZT* by experiments is 2.2 [27] in the nano-particle/nano-composites systems. It is experimentally observed that in both undoped nano-particles of $Bi_{1-x}Sb_x$ [14, 15] and $Bi_{1-x}Sb_x$ nano-particles doped with cerium and holmium [16, 17], all the thermoelectric related parameters can be controlled and improved by changing the particle size and defect distributions. Thus, more efforts should be put into develop the low temperature thermoelectric and cooling devices using $Bi_{1-x}Sb_x$ nano-particle/nano-composites systems.

However, there has not been a recent article discussing issues such as: what are the parameters introduced into different $Bi_{1-x}Sb_x$ nano-structures? What novel electronic properties does each type of structure have? What are some new, interesting research directions predicted for each type of nano-structured $Bi_{1-x}Sb_x$?

After a short introduction of bulk $Bi_{1-x}Sb_x$, this article reviews recent progress on research regarding the electronic properties for different types of nano-structured $Bi_{1-x}Sb_x$ materials, dividing the discussion into four topics:

(1) In the form of nanowires, parameters for the wire width, aspect ratio, and wire orientation are introduced, including strain effect along the wire. The resulting configuration of the carrier pockets can be arranged in many different ways, which result in interesting electronic phases.

(2) In the form of thin films, the parameters of film thickness and film orientation are introduced into the $Bi_{1-x}Sb_x$ materials. The quantum confinement effect is not as strong as it is for nanowires, which provides an opportunity to construct different types of Dirac cones, by taking advantage of the high degree of anisotropy, including exact-Dirac cones, semi-Dirac cones and quasi-Dirac cones, and also including single-Dirac cones, bi-Dirac cones and tri-Dirac cones. The two-dimensional form of the two-band model is introduced to handle the correlation between the dispersion shape and the mini-band gap under the quantum confinement effect. Moreover, in polycrystalline and mosaic-single-crystalline thin films, the distribution of the orientations of all the grains is also an important parameter that influences electronic behaviors.

(3) For the surface states of $Bi_{1-x}Sb_x$, the most recent important breakthrough has been the very first discovery of a topological insulator in the $Bi_{1-x}Sb_x$ system. Here we review the prediction of the existence of two different phases: the topologically trivial phase and the topologically non-trivial phase in the $Bi_{1-x}Sb_x$ system, the experimental measurement of these results, and the related theoretical explanations.

(4) In the form of nano-composites, the resulting materials have exhibited great flexibility, and this flexibility has provided a new direction for the enhancement of the thermoelectric performance of $Bi_{1-x}Sb_x$.

The unsolved problems for each type of nano-structured $Bi_{1-x}Sb_x$ will also be

mentioned at the end of each section.

1. Review of Bulk $Bi_{1-x}Sb_x$ Materials

1.1 Crystalline and Electronic Properties of $Bi_{1-x}Sb_x$

First we review progress made on studies of the electronic properties of bulk $Bi_{1-x}Sb_x$, which have been studied since the 1960s. Elemental bismuth and antimony are both in Column VA of the periodic table. The crystal structure of pure bismuth, pure antimony and their alloys is rhombohedral, which can be formed for a wide composition range of x and all have $R\bar{3}m$ symmetry, with two atoms in each unit cell, as shown in Fig. 1a. The lattice structure can be easily understood in terms of two inter-penetrating face centered cubic (FCC) sub-lattices elongated along the trigonal direction of the FCC diagonal to form crystalline $Bi_{1-x}Sb_x$. A natural Cartesian coordinate system is defined by this rhombohedral structure: the trigonal axis with C_3 symmetry, the binary axis with C_2 symmetry, and the bisectrix axis, which is perpendicular to both the trigonal axis and the binary axis. Because of the C_3 symmetry of the trigonal axis, it is also common for researchers to use a hexagonal notation to describe the different crystalline directions, where the trigonal axis, the binary axis and the bisectrix axis are denoted, respectively, by $[0001]$ $[1\bar{2}10]$ and $[10\bar{1}0]$, as shown in Fig. 1b. The lattice parameters of bulk $Bi_{1-x}Sb_x$ change monotonically with antimony composition x [28]. In terms of the hexagonal unit cell lattice parameters as shown in Table 1, *a* changes linearly with antimony composition *x,* and obeys Vegard's Law [28, 29]. However, the change in the lattice parameter *c* as a function of antimony composition

x deviates somewhat from the Vegard's Law. The lattice parameters for pure bulk bismuth and pure bulk antimony are listed in Table 1 [30, 31].

The electronic properties of bulk bismuth and bulk $Bi_{1-x}Sb_x$ alloys have interested researchers for many decades. Smith reported some detailed experimental results on the Hall effect and thermoelectric properties of $Bi_{1-x}Sb_x$ alloys as early as in 1911 [32]. Two decades later, Jones proposed a theoretical model for the electronic band structure of bismuth and $Bi_{1-x}Sb_x$ alloys based on Bloch theory [33], which was later extended to fit the galvanomagnetic experiments [34]. A magnetic field has been used for many years to measure the effective mass of electrons and holes in bismuth, antimony and $Bi_{1-x}Sb_x$ alloys [35-48]. Researchers have also found that the electronic band structure varies significantly as a function of temperature [28, 49], pressure[31, 50-58], magnetic field [59, 60], strain [61] and most importantly, stoichiometry [31, 62-64].

The first Brillouin zone for $Bi_{1-x}Sb_x$ can be seen as a Brillouin zone for the FCC lattice compressed along the trigonal axis, as shown in Fig. 1 c and d. For this distorted FCC lattice, there is only one *T* point, but three equivalent *L* points and six equivalent *H* points in the first Brillouin zone [28, 36]. The bottom of the conduction band is located at the *L* points. The top of the valence band for $Bi_{1-x}Sb_x$ can be located at the *T* point, the *L* points or the *H* points, depending on Sb composition [31, 62-64], temperature [28, 49], pressure [31, 50-58], magnetic field [59, 60] and stress [61]. The band structure does not change significantly as a function of temperature, when T is below the liquid nitrogen boiling point (77 K) and the sample is under atmospherical pressure. Figure 2 shows how the band edges at different high symmetry points change with antimony composition *x* in 3D bulk $Bi_{1-x}Sb_x$ alloys [63].

When $x < 0.07$, the valence band edge at the *T* point is above the conduction band edge at the *L* points, and bulk $Bi_{1-x}Sb_x$ is a semimetal. When $0.07 < x < 0.09$, the valence band edge at the *T* point is below the conduction band edge at the *L* points, but above the valence band edge at the *L* points, so that bulk $Bi_{1-x}Sb_x$ is an indirect-band-gap semiconductor. When $0.09 < x < 0.15$, the valence band edge at the *T* point and the valence band edge at the *H* points are both below the valence band edge at the *L* points, and bulk $Bi_{1-x}Sb_x$ in this composition range is a direct-band-gap semiconductor. When $0.15 < x < 0.22$, the valence band edge at the *H* points is above the valence band edge at the *L* points, but below the conduction band edge at the *L* points, so that bulk $Bi_{1-x}Sb_x$ in this composition range becomes an indirect-band-gap semiconductor again. When $x > 0.22$ the valence band edge at the *H* points is above the conduction band edge at the *L* points, so that bulk $Bi_{1-x}Sb_x$ becomes a semimetal.

The most interesting phenomenon for bulk $Bi_{1-x}Sb_x$ materials is that when $x < 0.04$ the *L*-point band gap decreases with antimony composition *x*, while when $x > 0.04$ the *L*-point band gap increases with antimony composition *x*. At $x = 0.04$ the conduction band edge and the valence band edge exchange their symmetries at the *L* points, and the *L*-point band gap E_g^L becomes zero, which leads to the formation of three symmetrical three dimensional (3D) Dirac points [28, 31, 64-67]. Under a strong magnetic field [68] or under hydrostatic pressure [69, 70], the value of the Sb composition x, where the Dirac point is formed, can be different from the value of x=0.04. The Sb composition becomes an important parameter in controlling the electronic structure.

1.2 Modeling of the Band Edges for Bulk $Bi_{1-x}Sb_x$

For exploring the electronic properties, researchers are interested in describing the band edges near the Fermi surface. Many efforts have been made on modeling the band structure of $Bi_{1-x}Sb_x$ alloys in bulk form. The valence band at the *T* point and at the *H* points are parabolically dispersed, while the valence band and the conduction band at the *L* points are non-parabolically dispersed, because of the strong interband coupling that occurs between the valence and conduction bands near the L point. It has been assumed that at the *L* point, only the carriers in the lowest conduction band and the highest valence band are important for the transport properties, and the dispersion relation for these energy bands near the *L* points can be well described by the Lax model [71, 72],

$$E(1+\frac{E}{E^L_{g,Bi,Bulk}})=\frac{\hbar^2}{2}\mathbf{k}\cdot\boldsymbol{\alpha}^L_{Bi,Bulk}\cdot\mathbf{k}\,, \qquad (1.1)$$

where $E^L_{g,Bi,Bulk}$ is the *L*-point band gap, and $\boldsymbol{\alpha}^L_{Bi,Bulk}$ is the three-dimensional tensor for the inverse-effective-mass for bulk bismuth. This model was proposed first for bulk bismuth based on $\mathbf{k}\cdot\mathbf{p}$ perturbation theory [73], and was later used in $Bi_{1-x}Sb_x$ alloys [72]. This non-parabolic model turned out to be valid for describing the electronic structure as probed by many subsequent experiments [42, 43, 74]. Its simplicity and its high accuracy made the Lax model have a high impact on the development of this field. This is also one reason why so many experiments were done on bulk Bi and bulk $Bi_{1-x}Sb_x$ in early days as a way to test band models, and models for the electronic structure generally.

To study the relation between the *L*-point band gap $E^L_{g,Bi,Bulk}$ and the inverse-effective-mass $\boldsymbol{\alpha}^L_{Bi,,Bulk}$, magneto-optical measurements were carried out by

many investigators, and we mention here as an example the work of Mendez et al [75, 76]. By making a regression fit of Mendez's magneto-optical data of $\boldsymbol{\alpha}^{L}_{Bi,,Bulk}$ as a function of $E^{L}_{g,Bi,Bulk}$ at different temperatures, it can be summarized that,

$$E^{L}_{g,Bi_{1-x}Sb_x,Bulk}\boldsymbol{\alpha}^{L}_{Bi_{1-x}Sb_x,Bulk} = (1 - xC_T)\cdot E^{L}_{g,Bi,Bulk}\boldsymbol{\alpha}^{L}_{Bi,Bulk}, \quad (1.2)$$

where C_T is a small dimensionless constant over the Sb composition x in the range of $0 < x < 0.3$, but changes somewhat as a function of temperature T, e.g. $C_{84\,\mathrm{K}} = 0.16$. To avoid all the complications of including C_T in Eq. (1.2), the further approximation that is normally made is $xC_T \ll 1$, which is generally valid for describing most experimental works, and has almost always been made for simplicity. Neglecting the term xC_T in Eq. (1.1), we obtain the scaling relation,

$$\boldsymbol{\alpha}^{L}_{Bi_{1-x}Sb_x} = \frac{E^{L}_{g,Bi}}{E^{L}_{g,Bi_{1-x}Sb_x}}\boldsymbol{\alpha}^{L}_{Bi}. \quad (1.3)$$

For the L point energy gap and the inverse effective mass, the empirical relation of Eq. 1.3 between $E^{L}_{g,Bi_{1-x}Sb_x}$ and $\boldsymbol{\alpha}^{L}_{Bi_{1-x}Sb_x}$ has been further discussed by Rabin et al [77], who has written a more complete expression for Eq. (1.3) [77], which can be used for higher resolution studies:

$$\boldsymbol{\alpha}^{L}_{Bi_{1-x}Sb_x} = \frac{E^{L}_{g,Bi}}{E^{L}_{g,Bi_{1-x}Sb_x}}[\boldsymbol{\alpha}^{L}_{Bi} - \frac{1}{m_0}\mathbf{I}] + \frac{1}{m_0}\mathbf{I}. \quad (1.4)$$

where m_0 is the mass of a free electron. Equation (1.4) and Rabin's result of Eq. (1.3)

and Mendez's empirical relation in Eq. (1.2) are all consistent with each other, as far as the term $m_0^{-1}\mathbf{I}$ is very small. Since the effective mass components of $Bi_{1-x}Sb_x$ are always 1 to 3 orders of magnitude smaller than m_0, this $m_0^{-1}\mathbf{I}$ term can be ignored in explaining almost all experimental observations for $Bi_{1-x}Sb_x$ samples where $x \leq 0.3$.

The three-dimensional model for bulk $Bi_{1-x}Sb_x$ in Eq. (1.1) and (1.2) has provided a base for the analysis of nano-structured $Bi_{1-x}Sb_x$ systems discussed below. The low-dimensional modeling of $Bi_{1-x}Sb_x$ is discussed in Section 3.

2. Nanowires of $Bi_{1-x}Sb_x$

By growing the $Bi_{1-x}Sb_x$ in the form of nanowires, quantum confinement is introduced in the directions that are perpendicular to the wire direction. This introduces the three parameters of the (1) wire orientation with respect to crystal axes, (2) the wire width and (3) the cross-section aspect ratio, which means the ratio between the long-side width and the short-side width of the cross-section, if the cross-section is rectangularly shaped (This aspect ratio is different from the ratio between the length of the nanowire and the width of its cross-section, if the cross-section is a square). This new set of parameters can be used to control the electronic behavior, and, in particular, the quantum confinement effect which has been recently used to improve the thermoelectric performance of $Bi_{1-x}Sb_x$ [3-5, 78].

Since the first synthesis of $Bi_{1-x}Sb_x$ nanowires by Lin et al. in 2001 [3, 18], the resistivity and conductivity as a function of stoichiometry, temperature, strain, etc. have been

studied by various researchers. Lin *et al.* prepared (012) oriented $Bi_{1-x}Sb_x$ nanowires with diameters 40 and 65 nm, and with Sb composition x=0, 0.05, 0.10, and 0.15. Resistance and magnetoresistance experiments over the temperature range of 2-300 K were carried out on these samples as shown in Fig. 3 [3]. It is here shown that the resistance increases as the temperature drops from room temperature to 2 K, and the resistance values saturate at low temperature below ~50 K. Lin et al. concluded on this basis that in the low temperature range, the nanowire resistance in their samples was dominated by carriers from ionized impurity levels, rather than from intrinsic $Bi_{1-x}Sb_x$ levels. The galvano-thermomagnetic properties at a phase transition induced by an anisotropic strain effect for $Bi_{0.92}Sb_{0.08}$ wires of larger diameters (0.3<d<5 μm) were studied by Nikolaeva et al [6, 7, 19]. The dependence of the resistivity ρ was found to have an exponential form and to be dominated by a thermal gap according to,

$$\rho = \rho_0 \cdot \exp(\frac{\Delta E_{TG}}{k \cdot T}) \qquad (1.5),$$

where ρ_0 is the resistivity at 4.2 K, and ΔE_{TG} is the thermal gap, which decreases with the longitudinal elastic strain ξ, as shown in Fig. 4 a. Furthermore, it was observed that the concentration of *L*-point holes in their samples increases as the strain ξ increases, as confirmed by the increased SdH oscillation amplitude with increasing magnetic field shown in Fig. 4 b. Under a $\xi = 0.2\%$ strain, no obvious signal of the SdH oscillation of *L*-point holes was observed, while the oscillation amplitude obviously increases when $\xi > 0.2\%$, which was interpreted in terms of a semiconductor-semimetal phase transition [19]. The overall behavior of the relative resistance $R(\xi)/R(\xi = 0)$, and the relative thermopower $\alpha(\xi)/\alpha(\xi = 0)$ as a function of strain ξ at different temperatures was also measured by the authors, as shown in Fig. 4 c and d. It was shown that for these large diameter wires, an increase

of the strain will reduce both the resistivity and the Seebeck coefficient, and therefore reduce the power factor, which is also consistent with the increased carrier concentration, as shown in the SdH experiment of Fig. 4 b. Despite the importance of this transport study [19], it did not give readers a systematic strategy on how to find the optimal value of strain to maximize the thermoelectric behavior at different temperatures.

Rabin et al [4] have theoretically studied the electronic phase diagram and the *ZT* for trigonal-oriented $Bi_{1-x}Sb_x$ nanowires (with an aspect ratio of 1), as a function of Sb composition x and wire diameters d, for $0<x<0.30$, 10 nm$<d<$100 nm and T=77 K, as shown in Fig. 5. The authors found that the Seebeck coefficient can be enhanced by aligning the *T*-point valence band-edge and the *L* point valence band-edges to the same value in energy. The prediction of a *ZT* as high as 2.5 suggested pursuit of this concept. These theoretical findings of Rabin *et al.* were soon investigated experimentally by Lin et *al* [5], as shown in the plot of the temperature dependence of the Seebeck coefficient for various Bi and $Bi_{0.95}Sb_{0.05}$ nanowires in Fig. 6. Tang et *al.* later provided a systematic theoretical study on the electronic phases and band gaps/overlaps of $Bi_{1-x}Sb_x$ nanowires as a function of growth orientation, stoichiometry and wire diameter. The electronic phase diagrams and maps of band gap/overlap as a function of stoichiometry and growth orientation for 10 nm thick $Bi_{1-x}Sb_x$ nanowires are illustrated in Fig. 6.5 [79], and the electronic phase diagram of $Bi_{0.95}Sb_{0.05}$ and $Bi_{0.87}Sb_{0.13}$ nanowires as a function of growth orientation and wire diameter are illustrated in Fig. 6.6 [79].

These theoretical and experimental studies have both left much work that has not yet

been done. From the fundamental end, the relation between the nanowire orientation and its electronic properties, including the electronic phase of the nanowires, the band gap/overlap, the electrical conductivity, the thermal conductivity, the Seebeck coefficient, and therefore the power factor and *ZT*, has not yet been investigated as a function of temperature and many of the other experimental parameters mentioned above. Such questions, however, are especially important and interesting for the $Bi_{1-x}Sb_x$ nanowire materials system, because of the high anisotropy of the $Bi_{1-x}Sb_x$, which makes its electronic properties very sensitive to the growth orientation. Nanowires with trigonal orientation and nanowires with bisectrix orientation are expected to have remarkably different electronic behaviors, as has been shown in the case of thin films as discussed in the next section. Furthermore, these electronic properties may also vary in an interesting way as a function of their aspect ratio. The electronic properties of nanowires with an aspect ratio that is different from 1 have not been studied yet. From an applications standpoint, since the results in Fig. 6 of Lin et al [5] have shown that the magnitude of the Seebeck coefficient for $Bi_{1-x}Sb_x$ nanowires can be increased by changing the diameter and the stoichiometry, the optimization of *ZT* for thermoelectricity generation and super-cooling applications still remains an open problem for future exploration. Moreover, since the band gap/overlap is always in the meV range, the design of infrared and terahertz devices by taking advantage of the controllability of the band gap/overlap is also remaining an interesting, largely unexplored, research direction.

3. Films of $Bi_{1-x}Sb_x$

Similar to the case of nanowires, thin films of $Bi_{1-x}Sb_x$ are also influenced by quantum confinement effects. However, the confinement is weaker in thin films than in nanowires, because the quantum confinement effect is limited to one direction, i.e. the film growth direction. Because the anisotropy of $Bi_{1-x}Sb_x$ film growth provides opportunities to use the confinement effect to break the symmetry of the bulk material, the mini-band gap/overlap in the small magnitude regime can be controlled, so that the ultra-high carrier mobility can be maintained. Furthermore, polycrystalline and single crystalline thin films provide opportunities for different research directions of interest, some of which are discussed in the following sub-sections.

3.1 Polycrystalline and mosaic-single-crystalline $Bi_{1-x}Sb_x$ films

Polycrystalline $Bi_{1-x}Sb_x$ films are easier to synthesize than single crystalline $Bi_{1-x}Sb_x$ films. However, the complexity of these polycrystalline systems and the difficulty to investigate them quantitatively are much larger. Polycrystalline $Bi_{1-x}Sb_x$ films were synthesized long ago by evaporation, even before the 1980s [80, 81]. Das et al. studied the temperature dependence of the electrical resistance, carrier density and carrier mobility of polycrystalline $Bi_{0.6}Sb_{0.4}$ films with film thicknesses 52 nm, 193 nm and 456 nm, over the temperature range of 100 to 1000 K [9, 82], in 1980 [9] and 2005 [53], respectively. Similar experiments for 250 nm $Bi_{0.5}Sb_{0.5}$ films doped with Te and Sn were later (1986) carried out by Takabe et al. from 77 to 300 K [83]. Völklein and Dillner studied (1990) the carrier mobilities and concentrations for polycrystalline $Bi_{0.87}Sb_{0.13}$ films with film thickness 30-300 nm at 80-360 K [84]. In 2011, Rogechava et al then synthesized the trigonal-orientated mosaic-single-crystal $Bi_{0.955}Sb_{0.045}$ films

with film thickness 10-300 nm, and studied the oscillations in the room temperature electrical conductivity, Seebeck coefficient, and Hall coefficient as a function of film thickness [10]. It was observed that the electrical conductivity, Seebeck coefficient, Hall coefficient, and thermoelectric power factor all tend to increase with film thickness in these samples, and oscillations were observed over a large range of film thickness, as shown in Fig. 9, where the measurements are shown for negatively doped $Bi_{1-x}Sb_x$ thin film samples. The oscillation period is found to be $\Delta d \approx 80\pm5$ nm. Usually, in other materials systems, the electrical conductivity and the Seebeck coefficient will show opposite trends of peaks and valleys. However, in Fig. 9 the electrical conductivity and the Seebeck coefficient as a function of film thickness are positively correlated, which is very abnormal. This could be due to a special rearrangement of all the thirteen different carrier pockets at the *T* point, the *L* points and the *H* points, or to a surface effect, or to grain boundary scattering. Thus, the importance of this work is that the abnormal positive correlation between electrical conductivity and Seebeck coefficient is found in the mosaic-single-crystal $Bi_{1-x}Sb_x$ thin films, which has provided a new inspiration on the problem of maximizing thermoelectric ZT. This abnormal behavior remains a very interesting future direction for the field.

Polycrystalline and mosaic-single-crystalline $Bi_{1-x}Sb_x$ films introduced several parameters to the system, including the grain size, defect distribution, grain orientation distribution, etc. that may be controlled besides the film thickness. The special characteristics of the grains associated with the growth process and with the quantum confinement effect of the films are both involved. The control possibilities significantly increase the flexibility of the electronic properties of $Bi_{1-x}Sb_x$ systems. On the other hand, the complexity of the problem is also highly increased, which

opens more research directions on how to harness the electronic behavior of these $Bi_{1-x}Sb_x$ films towards more functional applications.

Morelli et al. [8] first synthesized epitaxial $Bi_{1-x}Sb_x$ films of various Sb compositions x, following the techniques previously used by Partin et al. [85]. On this work, galvanomagnetic measurements were carried out to study the carrier concentration and mobility [8] at room temperature, as shown in Fig. 10 a-d. This work has provided three pieces of important information. First, ultra-high carrier mobilities were found with respect to those observed previously. Second, the band gaps for the synthesized thin films were found 1) to be larger, and 2) to increase faster with Sb composition than for bulk materials, at Sb compositions x=0, 1.97%, 5.6%, 8.7%, 10.3% and 12.3%, as shown in Fig. 10 e. These very nice results are consistent with the quantum confinement effect. Third, The most stable composition for structural stability appears at ~12% Sb, corresponding to the band peak in the curve in Fig. 10 e.

However, only ~1 μm thick films were synthesized in this work, and the films were only grown along the trigonal direction [8]. A more detailed study was later carried out by Cho et al. [86]. The successes of these works [8, 10, 86] provided the motivation for systematic studies of single crystal thin films of $Bi_{1-x}Sb_x$, because it is only if the films are single crystal, that the highly anisotropic properties of $Bi_{1-x}Sb_x$ can be fully explored and studied to show new phenomena that can be distinguished from behaviors observed for isotropic systems. Single crystalline $Bi_{1-x}Sb_x$ thin films turn out to be an interesting system for both fundamental physics studies and for applications. Recent progress with the study of single crystalline thin films of $Bi_{1-x}Sb_x$ are reviewed in the following sub-section.

3.2 Single crystalline $Bi_{1-x}Sb_x$ thin films

The first systematic study of the electronic band structure of single crystalline $Bi_{1-x}Sb_x$ thin films system was carried out by Tang and Dresselhaus [12]. Various types of Dirac cone states were found in the $Bi_{1-x}Sb_x$ thin films system [13]. The band gap, the band overlap and the related electronic phase diagrams have been systematically investigated [11], paying particular attention to the possibility of observing Dirac cones in $Bi_{1-x}Sb_x$ thin films and the conditions under which Dirac cones may occur.

3.2.1 Various types of Dirac cone states

Since the discovery of Dirac cones in monolayer graphene by Novoselov and Geim in 2004 [87], Dirac cone materials have recently attracted considerable attention, and researchers started looking for Dirac cones in other materials, including $Bi_{1-x}Sb_x$. A Dirac cone is a two-dimensional (2D) Dirac point. Dirac cone materials are interesting in electronic device design [88-90], quantum electrodynamics [89, 91], and in the design of desktop relativistic particle experiments [92-95].

First, the authors theoretically predicted that Dirac cone systems with different topological numbers can be constructed in the $Bi_{1-x}Sb_x$ thin film materials system. A Dirac cone materials system can be classified by its topological number: a single-, bi-, or tri-Dirac-cone system has, respectively, one, two or three degenerate Dirac cones in the first Brillouin zone. For example graphene is a bi-Dirac-cone system [88, 89, 96]. The surface of topological insulators [20] and of HgTe quantum wells [97] can be single-Dirac-cone systems. It is predicted that single-, bi- and tri-Dirac-cone materials

can be constructed from $Bi_{1-x}Sb_x$ thin films by using appropriate synthesis conditions to control the symmetry relations of the 3 *L* points [13]. The bisectrix oriented $Bi_{1-x}Sb_x$ thin films can be single-Dirac-cone materials, as illustrated in Fig. 11 a, because the quantum confinement effects differ significantly for the $L^{(1)}$-point carriers relative to the $L^{(2)}$- and $L^{(3)}$-point carriers due to the extreme anisotropy of the $Bi_{1-x}Sb_x$ crystal structure. Figure 11 b shows that a binary oriented $Bi_{1-x}Sb_x$ thin film can be a bi-Dirac-cone system, and Fig. 11c shows that a trigonal oriented film can be a tri-Dirac-cone system, where the orientation direction of these films is described in terms of the orientation of the film normal. Generally, the film grown normal to a crystalline direction in the $\hat{N}$-binary plane (Fig. 1d) can be a bi-Dirac-cone materials system; a film grown with no special symmetry would generally result in a single-Dirac-cone materials system.

Second, it is theoretically predicted that single-Dirac-cones of various degrees of anisotropy can be constructed in the $Bi_{1-x}Sb_x$ thin film systems. The degree of anisotropy for a single Dirac cone is defined by the authors in terms of the parameter $\gamma = |\mathbf{v}_{\max}|/|\mathbf{v}_{\min}|$ [13], where $\mathbf{v}_{\max}$ and $\mathbf{v}_{\min}$ stand for the maximum and minimum values of the in-plane carrier group velocities for this single Dirac cone. The group velocity is defined as $\mathbf{v}(\mathbf{k}_\square) = \hbar^{-1}\nabla_{\mathbf{k}_\square} E(\mathbf{k}_\square)$ [13]. Generally, the degree of anisotropy γ for a single *L*-point Dirac cone is plotted as a function of film growth orientation as shown in Fig. 12, which demonstrates that γ can be varied over a wide range of values (~2 to ~15) [13].

Two types of Dirac fermions associated with a Dirac cone are of interest: the massless

Dirac fermions and the massive Dirac fermions. The massless Dirac fermions exist right at the apex of a Dirac cone, with a zero-effective-mass m^*, due to the singularity of $E(\mathbf{k})$ at the apex of the Dirac cone. Other linearly dispersed Dirac fermions away from the apex of the Dirac cone are massive [12]. Tang and Dresselhaus proposed two main features to characterize the quality of an imperfect single Dirac cone as is observed in experiments: (1) the mini-mass for the "massless" Dirac fermions at the apex, and (2) the fermion group velocity $\mathbf{v}(\mathbf{k})$ for the massive Dirac fermions, as shown in Fig. 13.

The authors have also found how to construct a semi-Dirac-cone in a $Bi_{1-x}Sb_x$ thin film system as illustrated in Fig. 14, where the fermions are linearly dispersed along one direction and parabolically dispersed along another direction. The authors also pointed out that, by carefully controlling the film parameters, quasi-Dirac-cones with different magnitudes for the mini-band-gap can also be systematically constructed [11, 13].

This progress [11-13] with advancing our theoretical understanding has provided new directions for thin film synthesis, which urges research to be carried out on the synthesis of $Bi_{1-x}Sb_x$ thin films grown along crystalline directions with less symmetry than that along the trigonal axis. In particular, the method of constructing single-, bi- and tri-Dirac cones has provided a new research direction for studying the inter- and intra-valley scattering of Dirac fermions. The scattering of Dirac fermions in the graphene system has been studied in great detail. However, the graphene system has two symmetrical Dirac cones at the *K* point and at the *K*□ point. In many experiments the inter- and intra-valley scatterings are mixed together, and it is often difficult to

observe and study these phenomena separately. However, in the $Bi_{1-x}Sb_x$ thin film system that is here reviewed, the intra-valley scattering of Dirac fermions should be observable in single-Dirac cone thin films. In such films the inter-valley scattering between two Dirac cones, and between three Dirac cones should also be observable experimentally in bi-Dirac cone films and tri-Dirac cone films, respectively.

On the other hand, the proposal of anisotropic Dirac cones with a controllable degree of anisotropy and of a semi-Dirac cone can provide opportunities for research on Dirac fermion behaviors in anisotropic space, and can also mimic relativistic particles and help study anisotropic electrodynamics, which are all interesting fundamental topics. For application purposes, research on direction-selective electronic devices and on electronic direction-sensor development should also be launched, using the basic findings of the work reviewed here.

3.2.2 Band gap engineering and electronic phase diagrams

Due to the anisotropy of $Bi_{1-x}Sb_x$ thin films, the growth orientation has a remarkable influence on the symmetry properties of the various carrier pockets that will be created in these thin films and the electronic band structure, which will in turn affect the band structure. The symmetry properties of the carrier pockets and their influence on the band structure are found out and illustrated in Fig. 15, for three typical growth orientations.

Figures 15(a)-(c) show the carrier pockets of $Bi_{1-x}Sb_x$ thin films obtained by projecting the *T* point, the three *L* points and the six *H* points onto the film plane for

different growth orientations. These figures, as illustrated in Fig. 15(d)–(f), also show the symmetry properties of these projected carrier pockets, where the 100 nm thick films are chosen as examples.

The case, when the thin films are oriented along the trigonal axis, is shown in Fig. 15(a) and (d), where the C_3 symmetry of the three *L*-point carrier-pocket projections is retained, and where the C_6 symmetry and the inversion symmetry of the six *H*-point carrier-pocket projections is also retained. Thus, the bottom (top) of the conduction (valence) band is degenerate in energy at $L^{(1)}$, $L^{(2)}$, and $L^{(3)}$, and so is the top of the valence band at $H^{(1)}$, $H^{(2)}$, $H^{(3)}$, $H^{(4)}$, $H^{(5)}$, and $H^{(6)}$.

The case of the thin films oriented along the bisectrix axis is shown in Fig. 15 (b) and (e). In this case, the $L^{(2)}$-, the $H^{(2)}$-, and the $H^{(5)}$- point projections all have mirror symmetry with respect to the $L^{(3)}$-, the $H^{(3)}$-, and the $H^{(6)}$- point projections, respectively. The inversion symmetry of the *H* points is still retained in Figs. 15 (b) and (e). Figure 15 (e) shows that the bottom (top) of the conduction (valence) band at the $L^{(2)}$-point and the $L^{(3)}$-point projections are degenerate in energy, but are higher (lower) in energy than the $L^{(1)}$-point projection. The inversion symmetry ensures that the $H^{(j)}$ point is still degenerate in energy with respect to the $H^{(j+3)}$ points (j = 1, 2, or 3).

The case of the binary oriented $Bi_{1-x}Sb_x$ thin film is shown in Fig. 15 (c) and (f). In this case, the $L^{(2)}$-point projection and the $L^{(3)}$-point projection overlap, and are different from the $L^{(1)}$-point projection. The inversion symmetry of the *H* points is still retained. Meanwhile, the $H^{(2)}$- ($H^{(4)}$-) point carrier-pocket projections and the $H^{(3)}$-

($H^{(5)}$-) point carrier-pocket projections overlap with each other and are different from the $H^{(1)}$- ($H^{(6)}$-) point carrier-pocket projections. The inversion symmetry ensures that the $H^{(j)}$ point is degenerate in energy with the $H^{(j+3)}$ point (j = 1, 2, or 3).

The electronic phase diagram as a function of film thickness l and of antimony composition x for different growth orientations are calculated. The $Bi_{1-x}Sb_x$ thin-film system grown normal to the trigonal, bisectrix and binary axes are illustrated in Fig. 16 (a), (b) and (c), respectively. Region 1 and Region 5 are the semimetal phases, Region 2 and Region 4 are the indirect-gap semiconductor phases, and Region 3 is the direct-gap semiconductor phase. The top of the valence band is located at the T point for Region 1 and for Region 2, at the H points for Region 4 and Region 5, and at the L points for Region 3. The overall band-gap (positive) or band overlap (negative) as a function of film thickness and Sb composition is shown in Fig. 16 (d)-(f).

These results for the maps of the electronic phases, and band gap/overlap magnitudes have provided guidance for the synthesis of interesting $Bi_{1-x}Sb_x$ thin films. Investing the differences between the model in Fig. 16 and future experiments are of urgent interest. Based on the progress of the understanding of this class of materials, future research should be focused on how to engineer $Bi_{1-x}Sb_x$ thin films for specific functional applications. For cryogenic thermoelectrics, the controllability of the mini-band-gap at the L point and of the quasi-Dirac cones can provide new insights about how to increase the Seebeck coefficient, while maintaining the ultra-high mobility of the Dirac carriers (or quasi-Dirac carriers) in the $Bi_{1-x}Sb_x$ system, which could give a remarkable increase to the overall performance of thermoelectric generators and super-cooling devices in the cryogenic range. Furthermore, the thirteen

possible carrier pockets in $Bi_{1-x}Sb_x$ can be arranged in much more ways in thin films $Bi_{1-x}Sb_x$ than in bulk $Bi_{1-x}Sb_x$, so that the carrier concentration can be engineered with more flexibility.

3.2.3 Carrier concentrations

Tang and Dresselhaus calculated the intrinsic Fermi level of $Bi_{1-x}Sb_x$ thin films, when no doping is introduced and no gate voltage is applied [12]. The intrinsic Fermi level of a bisectrix oriented $Bi_{0.96}Sb_{0.04}$ film as a function of film thickness at the helium boiling point and nitrogen boiling point is illustrated in Fig. 17 (a). It can be seen that the semimetal-semiconductor phase transition occurs at around 40 nm, where the intrinsic Fermi level starts to drop as the film thickness decreases, which corresponds to the fact that the valence band at the T point falls below the conduction band which is located at the $L^{(1)}$ point (See Fig. 1).

The carrier concentration of $Bi_{1-x}Sb_x$ thin films as a function of film thickness and Fermi level has also been calculated. Figures 17 b and c illustrate the total carrier concentrations of a bisectrix oriented $Bi_{0.96}Sb_{0.04}$ thin film, at the helium boiling point and at the nitrogen boiling point, respectively. The overall carrier concentration is 10^{16} cm^{-3} at 4.2 K and an order of magnitude higher (10^{17} cm^{-3}) at 77 K.

Researchers have been trying to realize infrared devices and cryogenic meV electronics using Bi and $Bi_{1-x}Sb_x$ materials for many years. Recent studies on $Bi_{1-x}Sb_x$ thin films, and the guidance provided on how to control the band edges and the carrier

concentrations has opened more opportunities for advancing this research direction, and has also raised questions of how to harness all these parameters so that researchers could produce more useful devices.

4. Surface States of $Bi_{1-x}Sb_x$

The surface states of $Bi_{1-x}Sb_x$ have recently attracted intensive focus, after the first discovery of a topological insulator phase in $Bi_{1-x}Sb_x$ [20]. In 2007, Fu and Kane predicted that $Bi_{1-x}Sb_x$ with ($0.07<x<0.22$) would be a strong topological insulator, based on their calculations, showing that these materials would have topological metal surface states [21]: 1) There are an odd number of Dirac points in the surface states, i.e. the surface band structure is topologically non-trivial (the surface band structure is topologically trivial/non-trivial if the number of Dirac points is even/odd); 2) The topological insulator phase is robust against disorder. The region of the topological insulator in the phase diagram as a function of Sb composition x is shown in Fig. 18.

This result of Fu and Kane was observed in unpolarized ARPES experiments by Hsieh et al in 2008 [20] on the $Bi_{0.9}Sb_{0.1}$ (111) surface. Hsieh et al. measured the surface band structure below the Fermi energy of the $Bi_{0.9}Sb_{0.1}$ (111) surface along the $\bar{\Gamma}$ point to the $\bar{M}$ point, as shown in Fig. 19. Their results show that 1) the Fermi level is within the bulk gap of $Bi_{0.9}Sb_{0.1}$ (111); 2) there are five points (odd number) of crossings between the surface band structure and the Fermi level along the $\bar{\Gamma}$-$\bar{M}$ path; this observation was a breakthrough and proved the existence of a topological insulator phase [20]. Further details of experimental proofs from spin-polarized ARPES

experiments were later (2010) reported by Nishide et al [22].

After these breakthroughs, researchers began to give intensive focus to a clarification of the mechanisms behind the topological insulator phase in the $Bi_{1-x}Sb_x$ system. Teo et al. made a tight-binding calculation for the general $Bi_{1-x}Sb_x$ ($0.09<x<0.18$) (111) surface states and compared their predictions to the states deduced from experimental ARPES measurements [23]. Furthermore, Teo et al. predicted the locations of the Fermi level of the surface states for general $Bi_{1-x}Sb_x$ (111), (111)', (110) and (100) surfaces, as shown in Fig. 20.

Nakamura et al. later (2011) carried out an experimental study of the (111) surface states of $Bi_{1-x}Sb_x$ for three different Sb compositions (x=0.04, 0.07 and 0.21) [24]. The ARPES measured surface band structure of the (111) surfaces of $Bi_{0.96}Sb_{0.04}$ and $Bi_{0.79}Sb_{0.21}$ are shown in Fig. 21. Based on these results, Nakamura et al. summarized the scenario of the topological phase transition of the $Bi_{1-x}Sb_x$ (111) surface as a function of Sb composition x, which is described in Fig. 22. For non-alloyed Bi (x=0), there are two surface states Σ_1 and Σ_2, with opposite spin polarizations. Σ_1 and Σ_2 merge into the bulk *T*-point valence band at $\bar{\Gamma}$, and merge into the bulk *L*-point valence band at $\bar{M}$, and are topologically trivial, as shown in Fig. 22 a. When the Sb composition x increases to x=0.04, where the bulk valence band and the bulk conduction band touch each other at the *L* point, the surface Σ_2 band merges into the bulk *L*-point conduction band, instead of the bulk *L*-point valence band, and therefore, becomes topologically non-trivial, as shown in Fig. 22 b. For Sb composition larger than x=0.04, the surface bands Σ_1' and Σ_2' may split off from the Σ_1 and

Σ_2 bands, respectively. Σ_1 (Σ_1') has opposite spin orientations relative to Σ_2 (Σ_2'), and is topologically trivial, as shown by the solid lines in Fig. 22 c. The nontrivial bands Σ_2 and Σ_2' may hybridize with each other and form new bands at different Sb compositions, as shown by the dashed blue lines in Fig. 22 c, which reproduces the experimental result of Fig. 21.

The rise of interest in the $Bi_{1-x}Sb_x$ topological insulator has raised many new questions that need to be answered, e.g. what is the relation between the existence of a topological insulator phase and the strength of the spin-orbit interaction in the $Bi_{1-x}Sb_x$ system? Can a topological insulator phase be validated in other materials systems? These could be interesting questions for the understanding and development of novel spintronics. Zhang et al. [25] suggested that the existence of a topologically nontrivial phase is induced by changing the spin-orbit coupling strength when bismuth is doped with antimony. The authors [25] also suggested that the indirect bulk band gap, between the *L*-point electron pockets and the *T*-point hole pockets, can be controlled by uniaxial pressure along the trigonal axis, as shown in Fig. 23 [25]. Regarding control of the spin-orbit coupling strength by changing many parameters, such as the stoichiometry, strain, temperature, etc., this is still an emergent research direction that needs further exploration.

Another new research direction raised by the current progress is of emergent importance for applications, and this concerns the physical causes of the correlation between the existence of the topological insulator phase, and the performance of thermoelectrics in the $Bi_{1-x}Sb_x$ system, how this correlation can be controlled, and how this concept can be applied to other materials systems showing topological

phases. We can ask whether or not other topological insulators will show good thermoelectric performance? Researchers are currently making efforts to make progress along these research directions to answer the newly emerging questions.

5. Nano-Particles of $Bi_{1-x}Sb_x$

The topic of nano-particles of $Bi_{1-x}Sb_x$ consist of two aspects: the behavior of a single nano-particle and the behavior of bulk materials that are formed by nano-particles constituents. There has not yet been much research on the electronic properties of single nano-particles of $Bi_{1-x}Sb_x$. The research on bulk materials formed by nano-particles of $Bi_{1-x}Sb_x$ is also at a very early stage.

Before the explicit development of the nanotechnology field, researchers observed that the thermoelectric performance of polycrystalline $Bi_{1-x}Sb_x$ materials of micro-sized grains may change notably as a function of grain size [21, 22, 98, 99]. After the introduction of techniques such as ball milling, nano-sized particles of $Bi_{1-x}Sb_x$, were synthesized for the purpose of enhancing the figure of merit of thermoelectrics. Landschreiber et al. studied ZT for undoped nano-particles of $Bi_{1-x}Sb_x$ [14, 15], while Lukas et al. studied nano-particles of $Bi_{1-x}Sb_x$ doped with cerium and holmium [16, 17]. The works from Landschreiber et al. and Lukas et al. have confirmed that the electrical conductivity, the thermal conductivity and the Seebeck coefficient can be controlled as a function of particle size and defect distributions; the changing of electrical conductivity, the thermal conductivity and the Seebeck coefficient over the particle size and defect distributions follow different trends in both doped and undoped cases [14-17]. This confirms that synthesizing nano-particle/nano-composites of

$Bi_{1-x}Sb_x$ is a promising approach of low temperature *ZT* enhancement.

However, the figure of merit optimization problem becomes even more complicated and interesting in the case of nano-particles. More parameters are introduced into the materials system, including particle size distribution, different types of defects, each with different behaviors, particle orientation distributions, interface scattering and screening effect, etc. Researchers are making great efforts overall in optimizing the thermoelectric performance of the various promising thermoelectric materials, by controlled variation of the many parameters present in nano-particle thermoelectric materials, including stoichiometry, doping, external magnetic field, strain, temperature, etc. Nano-composites of Bi have mainly been synthesized to observe enhanced *ZT* by Heremans et al. [100], but more opportunity remains in investigation as a function of x, particle size, and temperature.

Furthermore, the phonon drag effect in the scattering mechanism is very important for cryogenic cooling, which has been extensively studied in the pure Bi systems by Issi et al [101-103]. However, this effect has not been yet studied in the nano-particles systems of $Bi_{1-x}Sb_x$, which could also be a promising research direction.

Conclusion

Due to recent developments of nanoscience and nanotechnology, the richness of anisotropic $Bi_{1-x}Sb_x$ materials appears to be a good candidate for renewed investigations for their special properties. The carrier pockets at the one *T* point, three *L* points and the six *H* points can be further engineered by exploring the special

properties of each type of nano-structure, taking advantage of size and shape dependence at the nanoscale. A much larger variety of electronic properties can in principle be achieved for different purposes of research and applications, but careful control of the size and orientation of the nano-structures is crucial for achieving the desired properties.

For nanowires of $Bi_{1-x}Sb_x$, there are strong quantum confinement effects, which change the electronic behaviors of the band edges differently at the *T* point, the *L* points and the *H* point. This provides an opportunity to align the thirteen carrier pockets in various ways. Both theoretical predictions and experimental results have shown that by properly changing the positions of each carrier pocket in energy, the thermoelectric figure merit *ZT* can, in principle, be enhanced, compared to its values in bulk $Bi_{1-x}Sb_x$. It is also found that *ZT* can be improved by changing the longitudinal strain along the nanowire. However, the optimization condition that has been found in theoretical calculations, where the nanowires oriented along the trigonal axis can have a ZT as high as 2.4, has not yet been synthesized experimentally. There has not yet been a theory showing how the strain changes the electronic and thermoelectric behaviors of $Bi_{1-x}Sb_x$ nanowires. Nor has the ultra-high anisotropy of $Bi_{1-x}Sb_x$ been fully exploited. It is likely that the growth orientation and the aspect ratio of nanowires may show significant influence on the electronic and thermoelectric behaviors, and many aspects of importance. In particular, less is known about the phonon behavior than about the electronic behavior, either theoretically or experimentally.

For single crystal thin films of $Bi_{1-x}Sb_x$, the weaker quantum confinement, compared

to the nanowire case, has provided an opportunity to break the symmetry of the three L points and still maintain the ultra-high carrier mobility. Various types of Dirac cone materials have been found, including Dirac cone materials with different numbers of valleys, quasi-Dirac cone materials with different magnitudes of their mini-band gaps, and semi-Dirac cones with different dispersion relations along different directions. Furthermore, the map of the electronic phases, including semi-metals, direct gap semi-conductors and indirect gap semi-conductors, and the map of band gap/overlap, of single crystal thin films of $Bi_{1-x}Sb_x$, as a function of film growth orientation, film thickness and stoichiometry, have been studied. New investigations are needed to study the scattering of Dirac fermions, e.g. the intra-valley scattering of fermions near a single Dirac cone, the inter-valley scattering between two/three Dirac cones, and the scattering at anisotropic Dirac cones and semi-Dirac cones. Investigations on novel phenomena that have been observed in the isotropic bi-Dirac cones in graphene can be also be carried out in the anisotropic Dirac cones in $Bi_{1-x}Sb_x$ thin films, such as the Klein paradox, the abnormal quantum Hall effect, etc. Because of the larger flexibility of the band structure and electronic properties of $Bi_{1-x}Sb_x$ thin films compared to bulk $Bi_{1-x}Sb_x$, studies in the fields of meV electronics, infrared sensors, and cryogenic thermoelectrics that are interesting in bulk $Bi_{1-x}Sb_x$ become much more attractive in $Bi_{1-x}Sb_x$ thin films.

For polycrystal and mosaic-single crystalline thin films of $Bi_{1-x}Sb_x$, oscillations have been observed in the electrical conductivity, Seebeck coefficient, and Hall coefficient, as a function of film thickness, where the electrical conductivity and the Seebeck coefficient were found to have an abnormal positive correlation. The reason for this abnormal correlation has not yet been studied in detail. It is still not known whether

this electronic behavior will change as a function of grain size distribution and grain orientation distribution.

For the surface states of $Bi_{1-x}Sb_x$, the topological insulator phase has been predicted and observed on the surface of polycrystalline $Bi_{1-x}Sb_x$. The correlations between the stoichiometry, the spin-orbit coupling, and the existence of a topological insulator phase have all been studied. However, it should be more interesting to study the possibility of a topological insulator phase in low-dimensional $Bi_{1-x}Sb_x$. Furthermore, it is also attractive to investigate the correlation between the thermoelectric performance and the existence of a topological phase in the $Bi_{1-x}Sb_x$ system.

For nano-particles of $Bi_{1-x}Sb_x$, it has been observed that the synthesis conditions of nano-particles will remarkably change the electronic properties of bulk materials formed by nano-particles of $Bi_{1-x}Sb_x$. The study of both single nano-particles and nano-composite bulk materials composed of compacted of nano-particles is still at an early stage of development. For the single nano-particle, it is not yet known how the electronic bands are changed under three-dimensional quantum confinement and what role the surface of a single nano-particle plays in its electronic behavior. For bulk materials formed by nano-particles of $Bi_{1-x}Sb_x$, it is not known how the distribution of particle size, grain boundary conditions, the distribution of particle orientations, etc. will influence the overall electronic behavior, nor are the optimal conditions known for enhancing the thermoelectric figure of merit *ZT*. For these systems, theoretical models are needed to guide the synthesis, and more samples synthesized under different conditions need to be measured, and then these results need to be systematically integrated with theoretical studies. Nano-composites of $Bi_{1-x}Sb_x$

nano-particles should be synthesized and compared with theoretical models to study the probability of further enhancing the thermoelectric *ZT*, as Heremans et al [100] observed in Bi nano-composites. Besides the electronic band structure, various scattering mechanisms, e.g. the phonon drag effect, boundary screening effect, etc., are very important, and need to be investigated in more detail for nano-composites.

Acknowledgement

S.T. and M.S.D. thank Prof. Jean-Paul Issi, Prof. Jean-Christophe Charlier, Prof. Joseph Heremans, Dr. Albert Liao and Dr. Hyungyu Jin, Dr. Yu-Ming Lin, Prof. Cyril Opeil, Prof. Oded Rabin, Dr. Art Edwards, Prof. David Hsieh, and Prof. Liang Fu for valuable discussions. The authors acknowledge the support from AFOSR MURI Grant number FA9550-10-1-0533, subaward 60028687, and the support from NSF-DMR-1107339 and CRDF-UKP2-7074-KK-12 for collaborative studies with Prof. Elena Rogacheva at the National Technical University "Kharkiv Polytechnic Institute". The views expressed in this article are not endorsed by the sponsor.

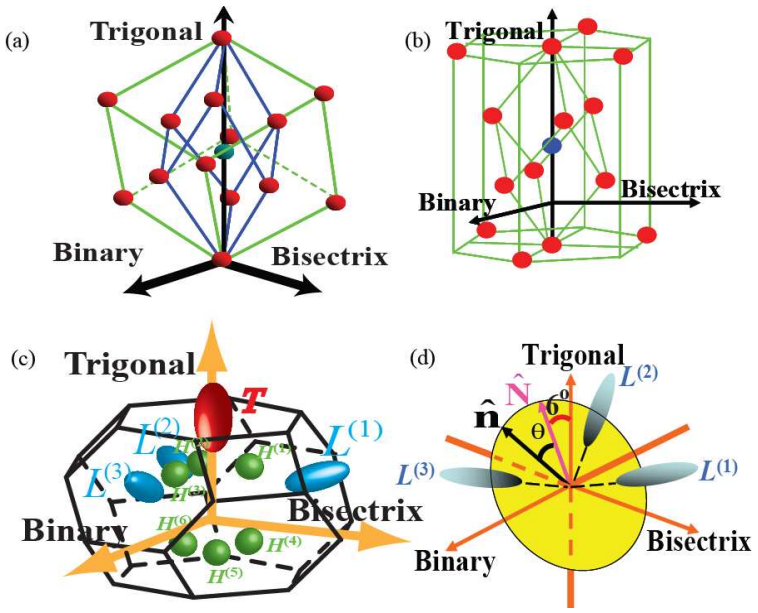

Fig. 1: [Reproduced from [11-13]] Structures of bulk bismuth antimony materials [11-13]. (a) The atomic structure of the rhombohedral structure of bismuth and antimony under a distorted cubic system. (b) The rhombohedral atomic structure of bismuth and antimony under a hexagonal framework. (c) The carrier pockets at the *T* point, the three L points and the six *H* points in the first Brillouin zone of bulk bismuth antimony. (d) Because of the band symmetry of the conduction band and the valence band at the *L* points, the hole-pocket and the electron-pocket at an *L* point can be considered as having similar axes and strongly coupled bands in *k*-space. The longest principal axes of the $L^{(2)}$- ellipsoid and $L^{(3)}$-point ellipsoid, together, form a plane, whose normal is denoted by the unit vector $\hat{N}$. The angle between the trigonal direction and the $\hat{N}$ is ~6°. $\hat{n}$ is a direction vector that lies in the plane that is normal to $\hat{N}$. The angle between $\hat{n}$ and $\hat{N}$ is θ.

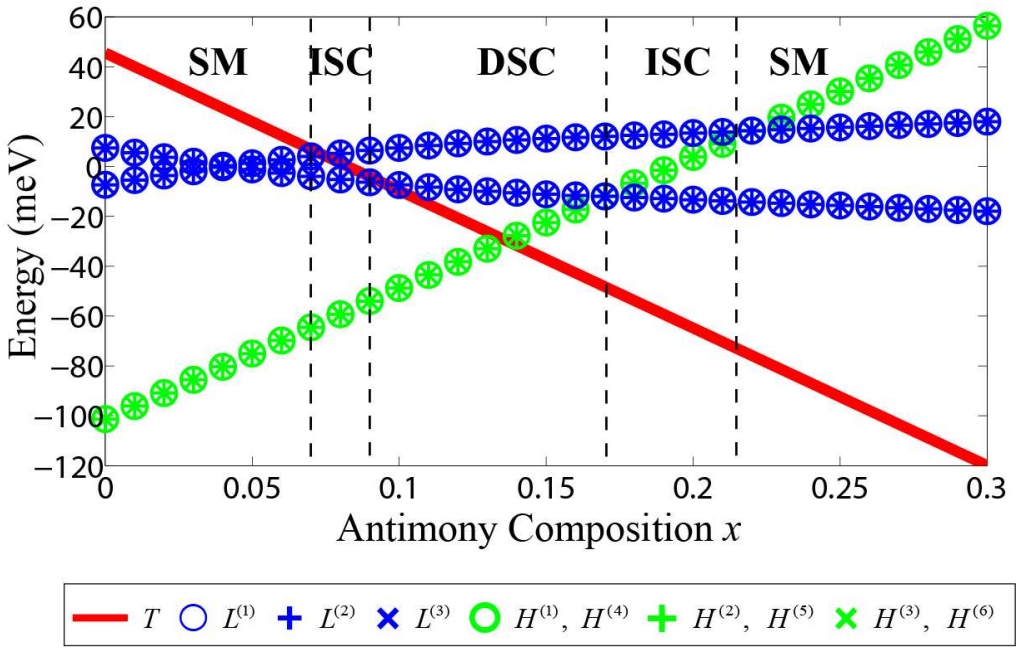

Fig. 2: [Reproduced from Ref. [11]] The energy of band edges at different symmetry-points in the first Brillouin zone as a function of Sb composition for bulk $Bi_{1-x}Sb_x$ [11]. Different electronic phase regions are marked as a function of x, including the semimetal (SM), indirect-semiconductor (ISC), and direct-semiconductor (DSC) phases.

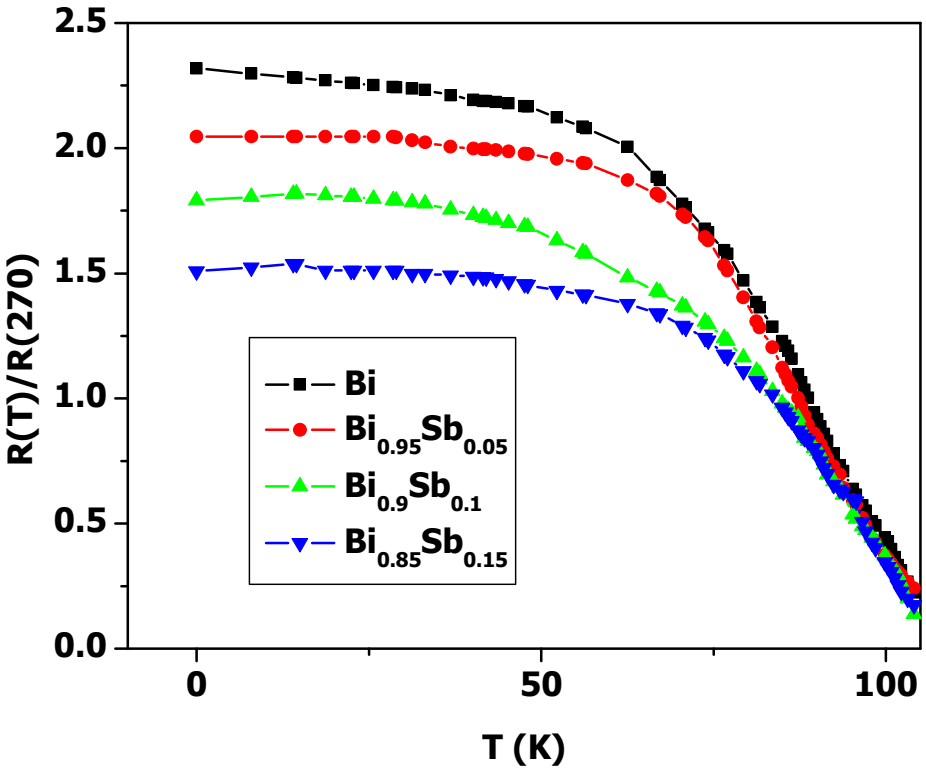

Fig. 3: [Reproduced from Ref. [3]] Normalized resistance as a function of temperature [3] $R(T)/R(270\ K)$ for $Bi_{1-x}Sb_x$ nanowires of a thickness of 40 nm, and with various Sb compositions $0 \le x \le 0.15$.

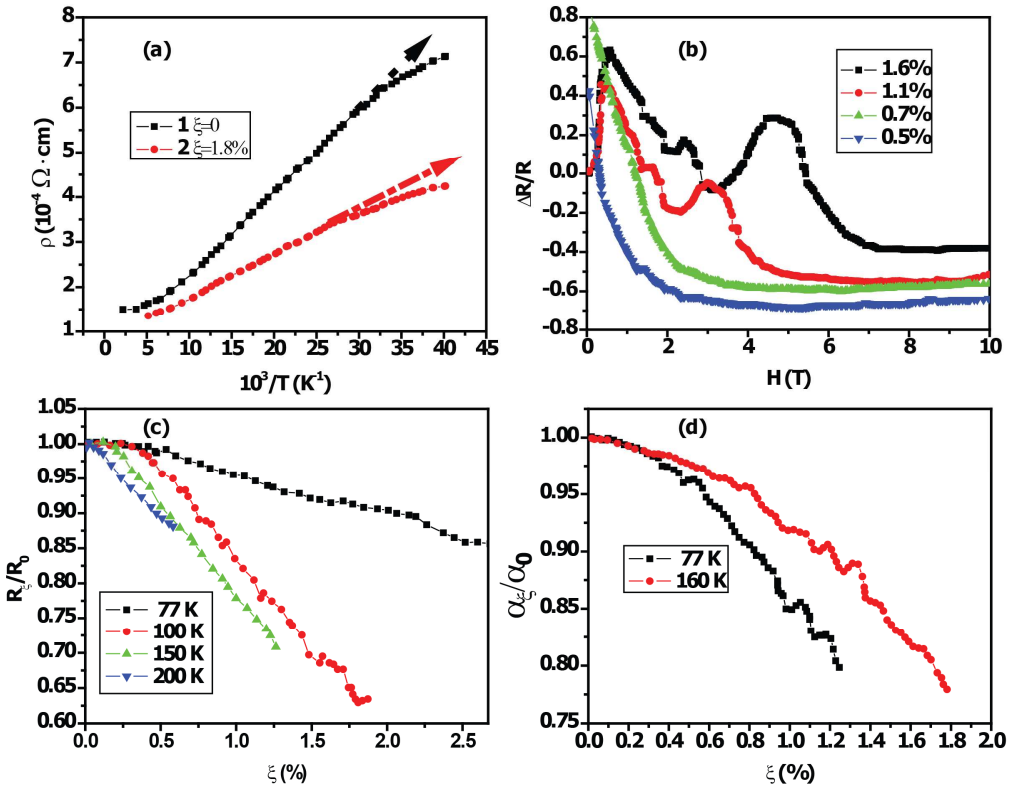

Fig. 4: [Reproduced from Ref. [19]] Electronic transport of $Bi_{0.92}Sb_{0.08}$ wires with diameters d=2 μm under different uniaxial strains [19]. (a) The resistivity ρ as a function of temperature for before and after application of uniaxial strain ξ as indicated. (b) The L-point-pocket SdH oscillation experiments carried out at different uniaxial strains ξ. (c) The relative resistance $R(\xi)/R(\xi=0)$ as a function of strain ξ at different temperatures T. (d) The relative thermo-power factor $\alpha(\xi)/\alpha(\xi=0)$ as a function of strain ξ at different temperatures.

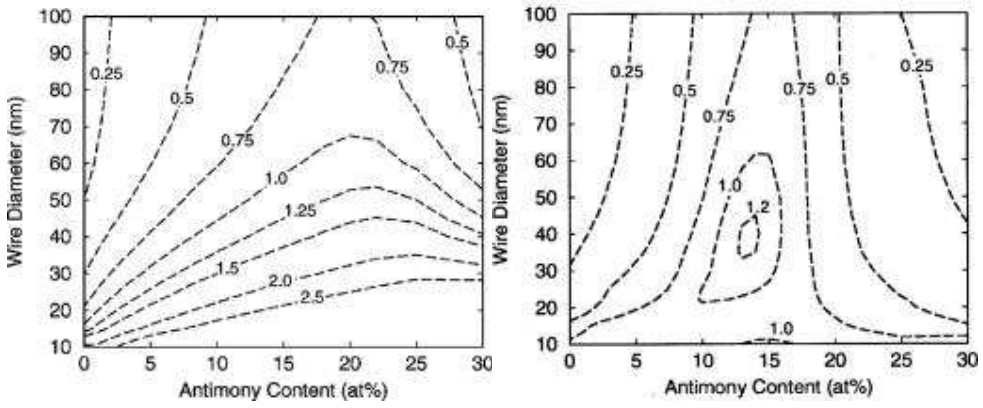

Fig. 5: [Reproduced from Ref. [4]] Contour plot of the calculated optimal *ZT* values [4] for (a) *n*-type and (b) *p*-type $Bi_{1-x}Sb_x$ nanowires as a function of Sb composition and wire diameter.

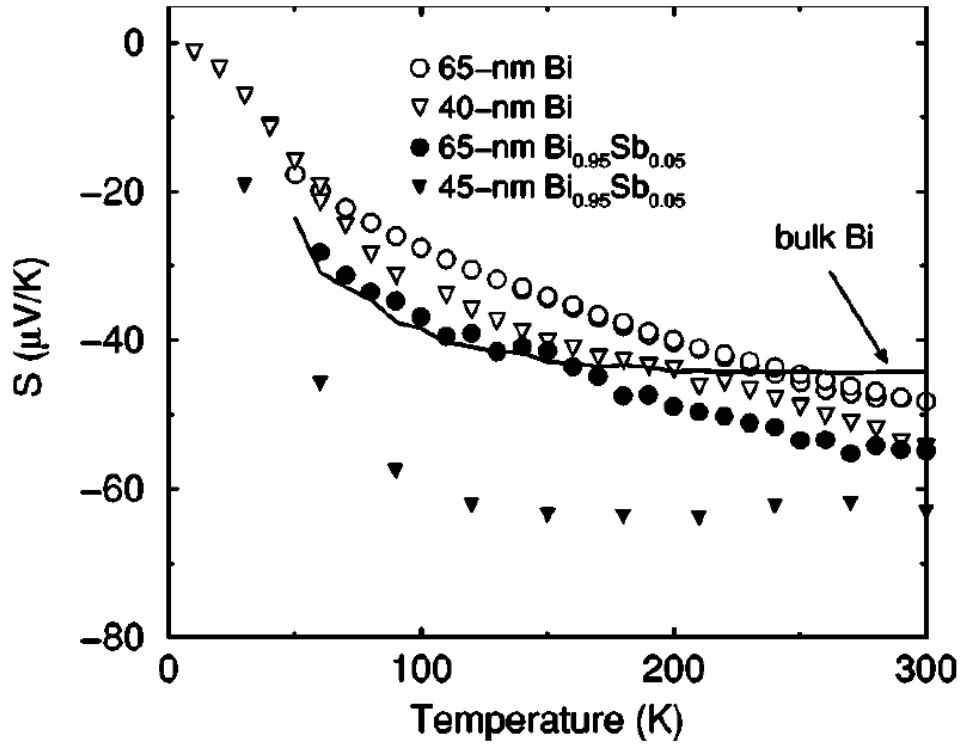

Fig. 6: [Reproduced from Ref. [5]] The Seebeck coefficient for Bi (○ , ▽) and $Bi_{0.95}Sb_{0.05}$ (● , ▼) nanowires with different diameters as a function of temperature from 2-300 K, compared to that for bulk Bi [5].

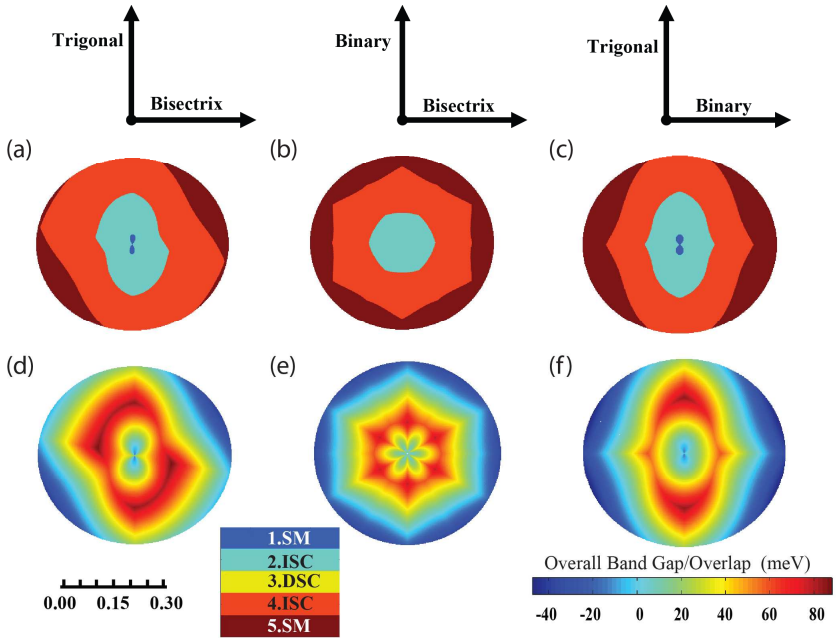

Fig. 7: [Reproduced from Ref. [79]] The electronic phase diagrams are shown in (a)-(c), and the maps of band gap/overlap are shown in (d)-(f) for 10 nm thick $Bi_{1-x}Sb_x$ nanowires, as a function of Sb composition and growth orientation. (a) and (d), (b) and (e), and (c) and (f) are for the cases where the growth orientation varies within the trigonal-bisectrix plane, the binary-bisectrix plane and the trigonal-binary plane, respectively. The circular diagrams are obtained as follows: first, a three-dimensional diagram of the electronic phase (or of the band gap/overlap) is plotted as a function of Sb composition and growth orientation, where at each point, the Sb composition is represented by the distance between this point and the origin, and the growth direction is represented by the vector starting from the origin and pointing to this point. Then the cross-sections of the spherical phase diagram (or band gap/overlap diagram) of the trigonal-bisectrix plane, the binary-bisectrix plane and the trigonal-binary plane are taken, as shown in (a), (b) and (c) (or in (d), (e) and (f)), respectively. Region 1 and Region 5 are semimetal phases, Region 2 and Region 4 are indirect gap semiconductor phases and Region 3 is direct gap semiconductor phases. The top of

the valence band is located at the *T* point in Region 1 and 2, at the *L* points in Region 3, and at the *H* points in Region 4 and 5. In (c), (d) and (e), a band gap and a band overlap are represented by a positive value and a negative value, respectively.

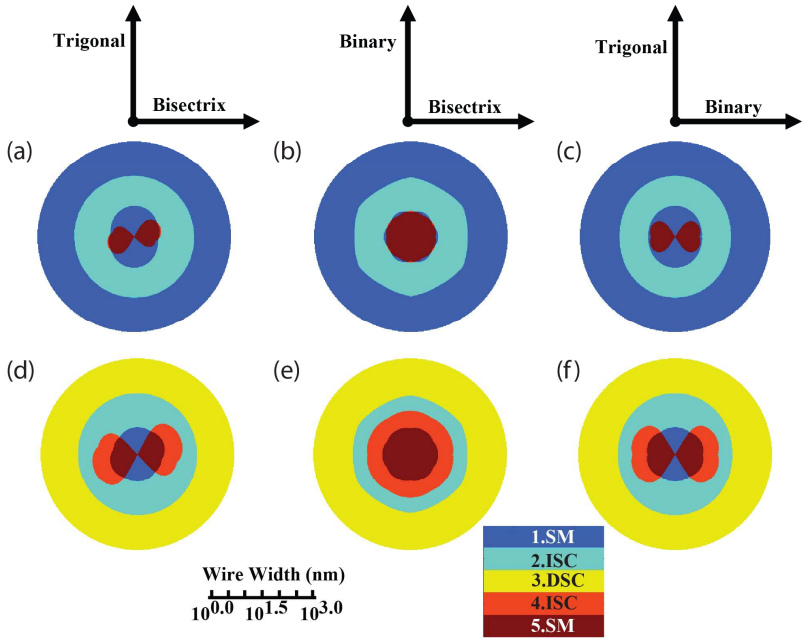

Fig. 8: [Reproduced from Ref. [79]] The electronic phase diagrams of $Bi_{0.95}Sb_{0.05}$ (a)-(c) and $Bi_{0.87}Sb_{0.13}$ (d)-(f) nanowires, as a function of diameter and growth orientation. The notations and legends in Fig. 7 (a)-(c) are used here, except that the length of the radius here represents the wire diameter, which is plotted on a logarithmic scale.

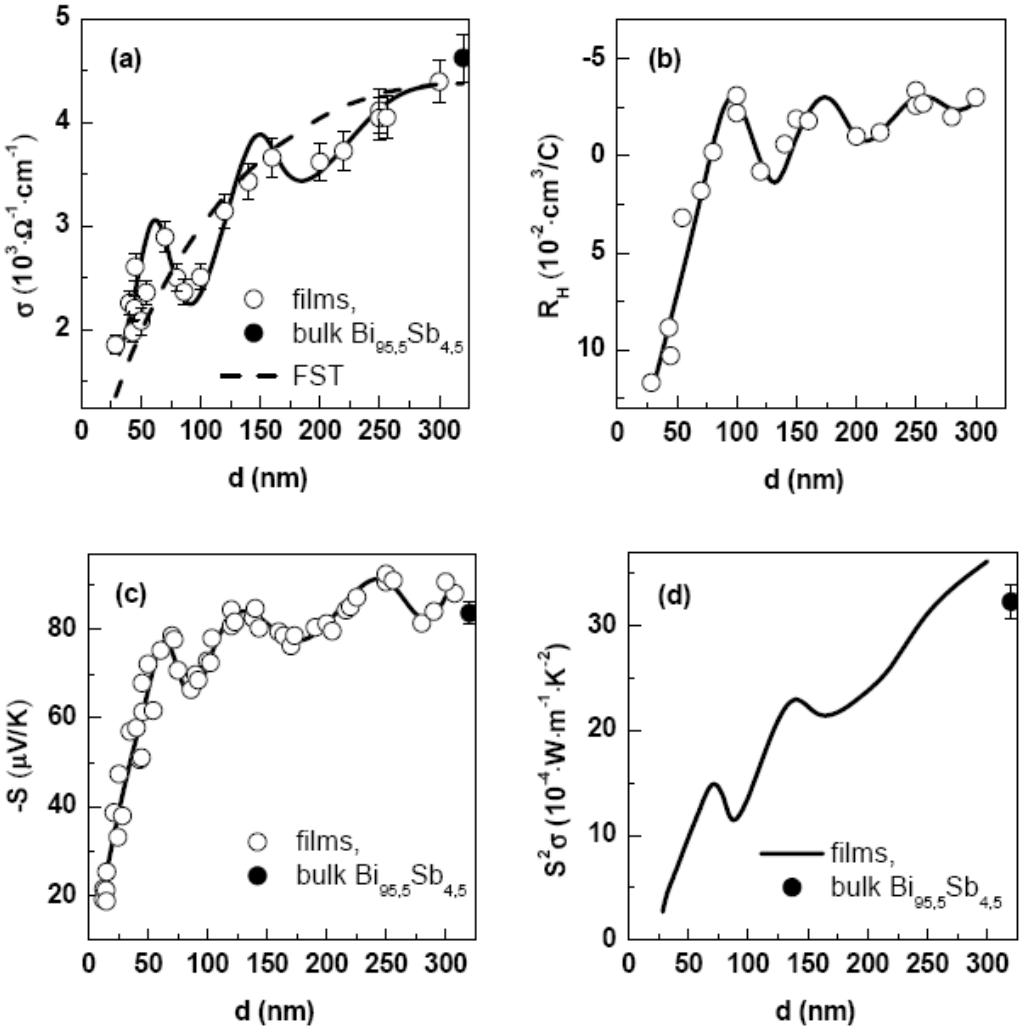

Fig. 9: [Reproduced from Ref. [10]] Quantum oscillations of the (a) electrical conductivity, (b) Hall coefficient, (c) Seebeck coefficient and (d) thermoelectric power factor vs. film thickness of $Bi_{0.955}Sb_{0.045}$ mosaic films at the room temperature [10].

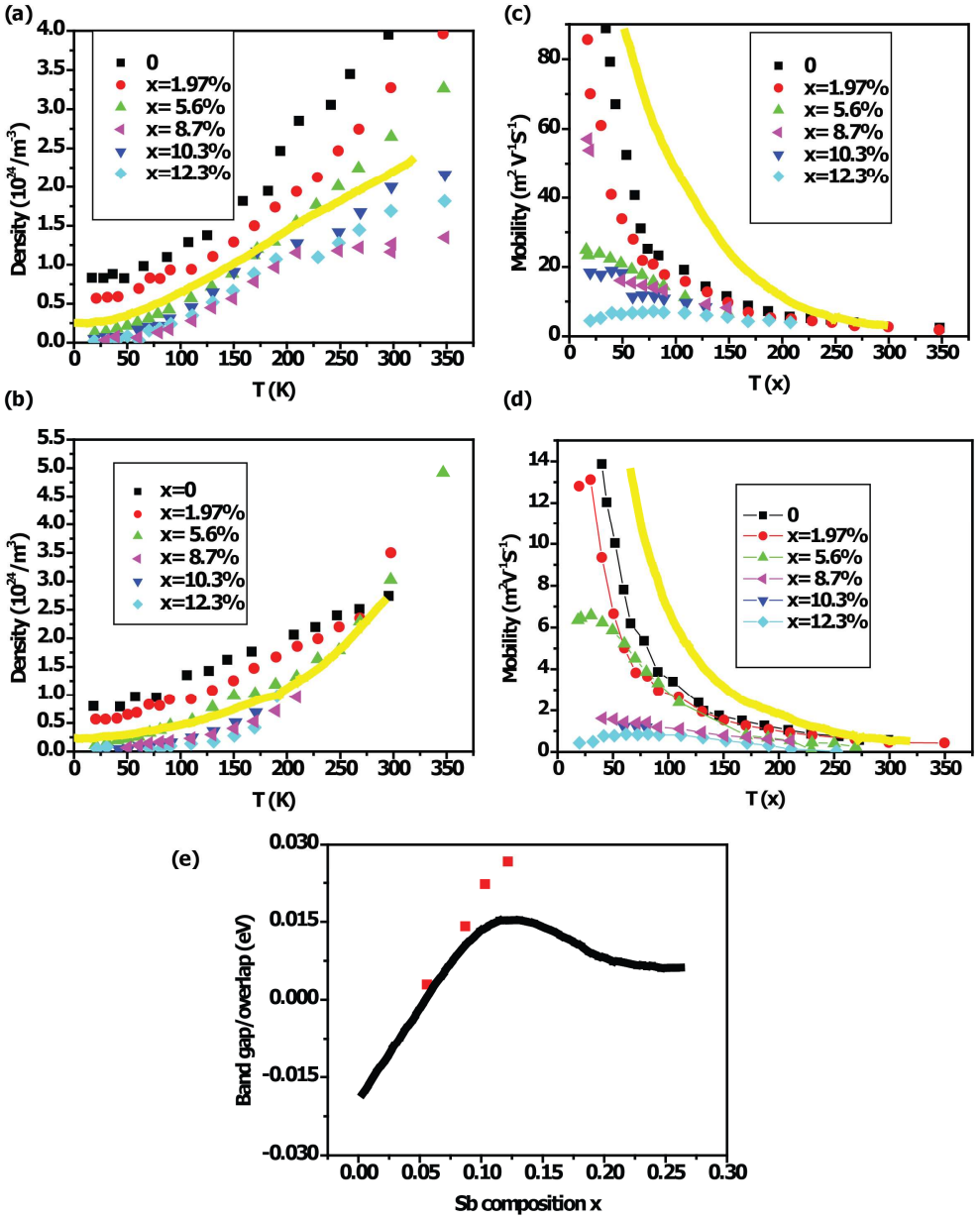

Fig. 10: [Reproduced from Ref. [8]] Measurements of densities vs. temperature of (a) electrons and (b) holes, and the mobilities vs. temperature of (c) electrons and (d) holes in ~1 μm thick $Bi_{1-x}Sb_x$ films for different Sb compositions x. The yellow solid line stands for bulk single crystal Bi. (e) The energy gap values for measured films (red square dot) compared to bulk (black solid line) of $Bi_{1-x}Sb_x$ as a function of Sb composition [8].

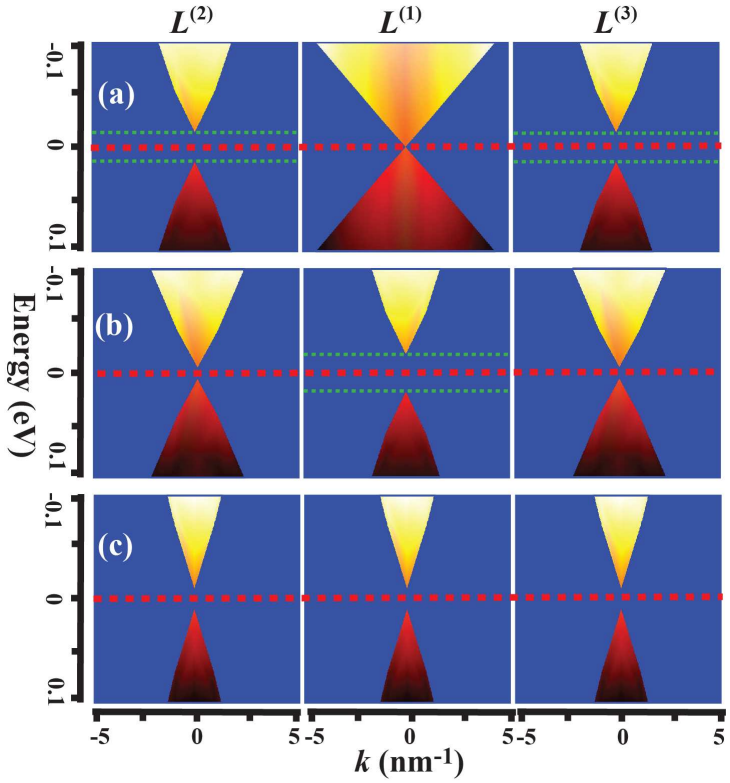

Fig. 11: [Reproduced from Ref. [13]] An illustration of (a) single-, (b) bi- and (c) tri-Dirac-cone $Bi_{1-x}Sb_x$ thin films that are grown normal to the (a) bisectrix, (b) binary and (c) trigonal directions, respectively [13].

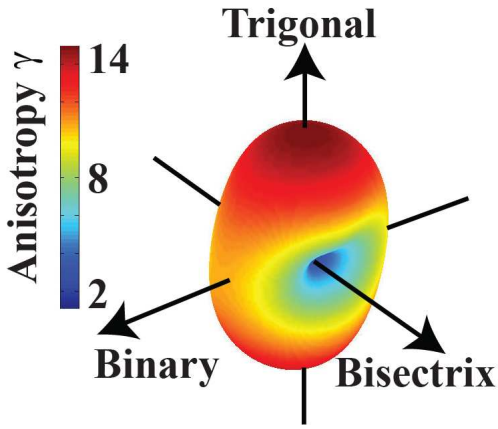

Fig. 12: [Reproduced from Ref. [13]] Scheme of the degree of anisotropy $\gamma = |\mathbf{v}_{max}|/|\mathbf{v}_{min}|$, where $\mathbf{v}_{max}$ and $\mathbf{v}_{min}$ stand for the maximum and minimum values of the in-plane carrier group velocities for this single Dirac cone, which is defined as $\mathbf{v}(\mathbf{k}_{\square}) = \hbar^{-1}\nabla_{\mathbf{k}\square}E(\mathbf{k}_{\square})$ for the $L^{(1)}$-point Dirac cone as a function of the film growth orientation. The magnitude of γ for a specific $Bi_{1-x}Sb_x$ thin film growth orientation is shown by the radius and color [13] on the color scale shown on the left.

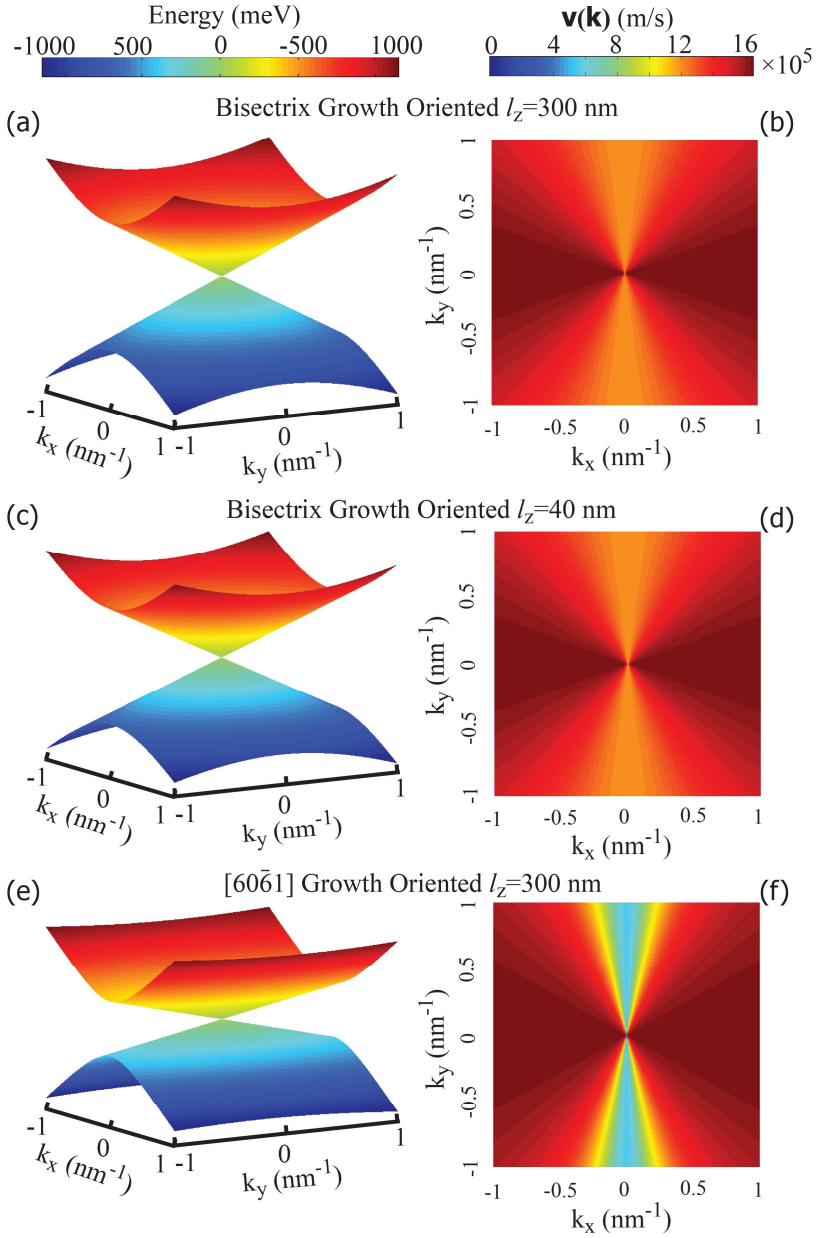

Fig. 13: [Reproduced from Ref. [12]] Different anisotropic single-Dirac-cones in different $Bi_{0.96}Sb_{0.04}$ thin films: (a) and (b) denote a sharp-apex $L^{(1)}$-point anisotropic single-Dirac-cone in a 300 nm thick bisectrix oriented $Bi_{0.96}Sb_{0.04}$ film. (c) and (d) denote an $L^{(1)}$-point anisotropic single-Dirac-cone in a 40 nm thick $Bi_{0.96}Sb_{0.04}$ bisectrix oriented film. (e) and (f) denote a highly anisotropic single-Dirac-cone in a 300 nm thick $Bi_{0.96}Sb_{0.04}$ film [60$\bar{6}$1] oriented film. (a), (c), and (e) show the dispersion relations. (b), (d), and (f) show the group velocities distribution [12].

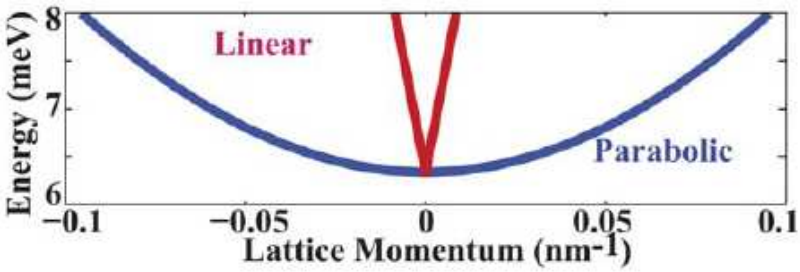

Fig. 14: [Reproduced from Ref. [13]] A semi-Dirac cone dispersion in a 100 nm thick $Bi_{0.9}Sb_{0.1}$ thin film system. The fermions have a parabolic dispersion relation along the v_{min} direction, and a linear dispersion relation along the v_{max} direction [13].

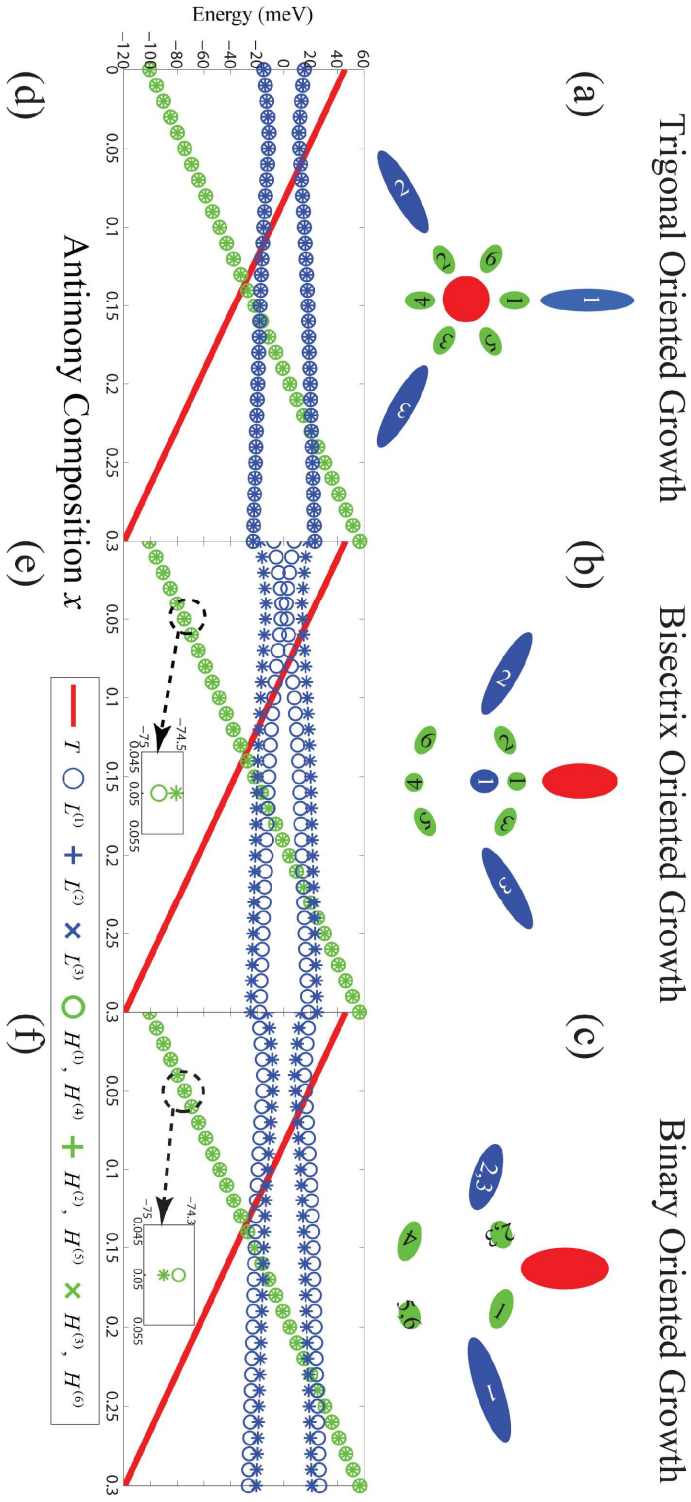

Fig. 15: [Reproduced from Ref. [11]] Schemes of the symmetry properties of the T-point (red), L-point (blue) and H-point (green) carrier pocket projections onto the film plane for $Bi_{1-x}Sb_x$ thin films for the (a) trigonal, (b) bisectrix and (c) binary

growth orientations. How such symmetry properties affect the relation of band-edge energy as a function of Sb composition is illustrated for 100 nm thick $Bi_{1-x}Sb_x$ thin films of (d) trigonal, (e) bisectrix and (f) binary growth orientations [11].

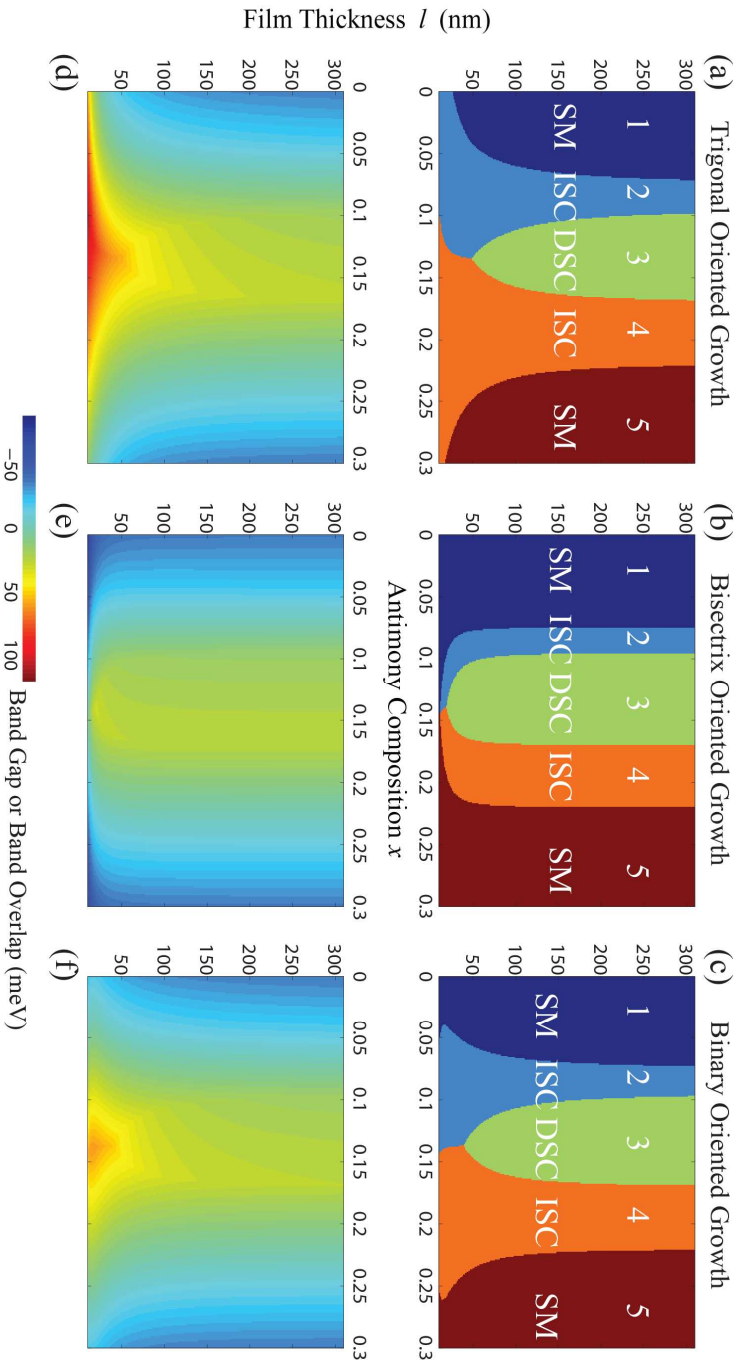

Fig. 16: [Reproduced from Ref. [11]] Phase diagrams for the $Bi_{1-x}Sb_x$ thin-film systems grown normal to (a) the trigonal axis, (b) the bisectrix axis, and (c) the binary axis, as a function of antimony composition x and film thickness l. The band gap/overlap map shown in (d), (e), and (f), are corresponding to (a), (b), and (c), respectively. A

positive value stands for a band gap, a negative value stands for a band overlap, and a zero value stands for a gapless state [11].

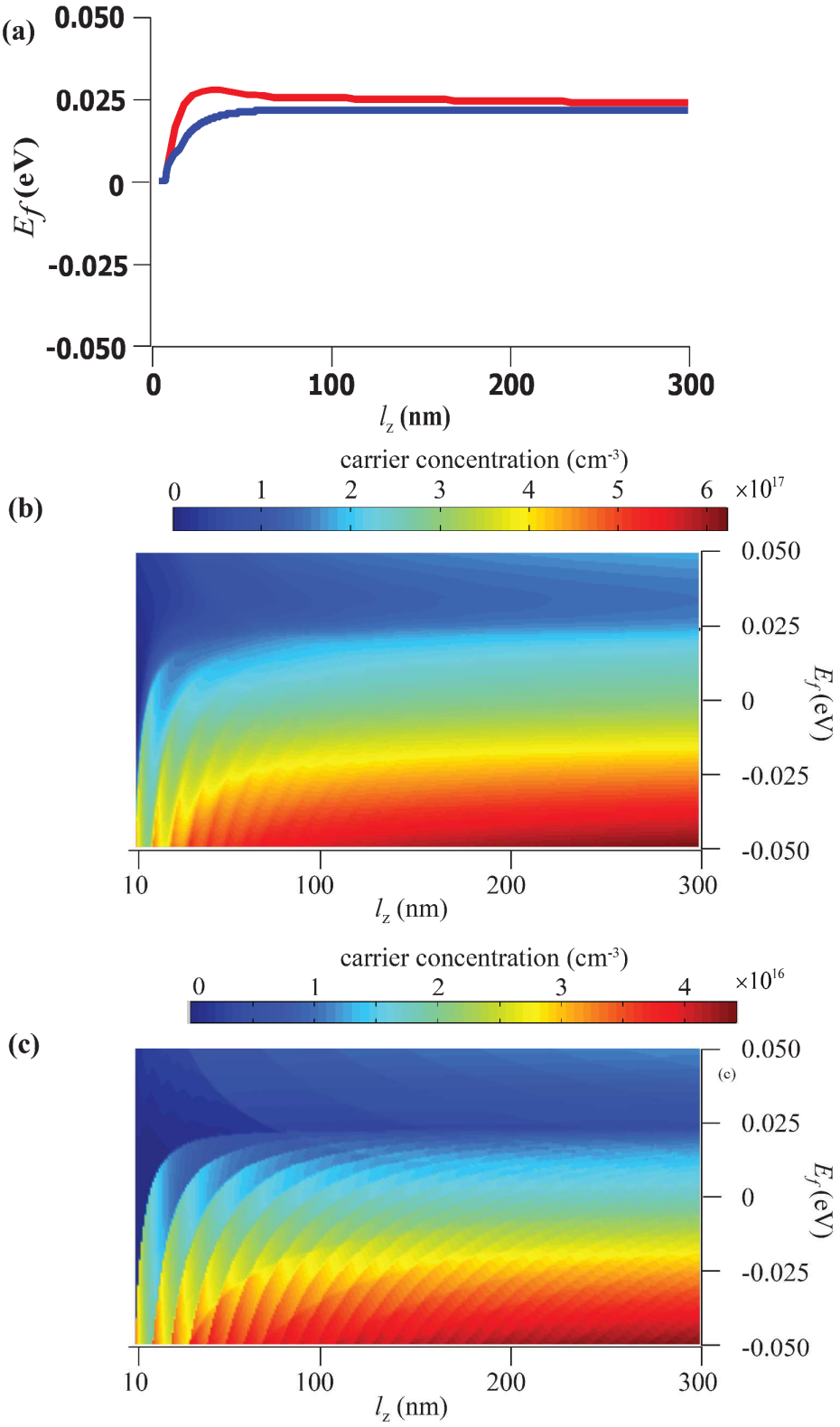

Fig. 17: [Reproduced from Ref. [12]] (a) The intrinsic Fermi level as a function of film thickness for bisectrix oriented $Bi_{0.96}Sb_{0.04}$ thin films, when no doping is added and no

gate voltage is applied, at 4.2 K (blue curve) and at 77 K (red curve). The carrier concentrations of as a function of film thickness and Fermi level are shown in (b) at 77 K and in (c) at 4.2 K [12].

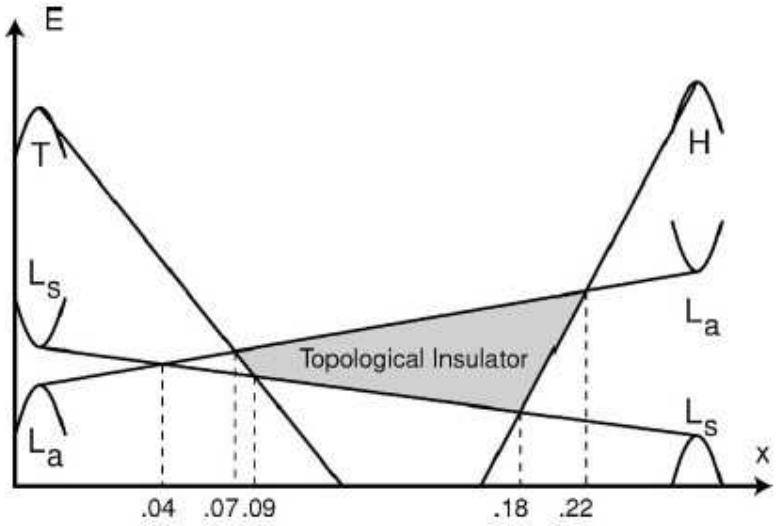

Fig. 18: [Reproduced from Ref. [21]] Phase diagram of topological metal surface states that exist in $Bi_{1-x}Sb_x$ alloys [21].

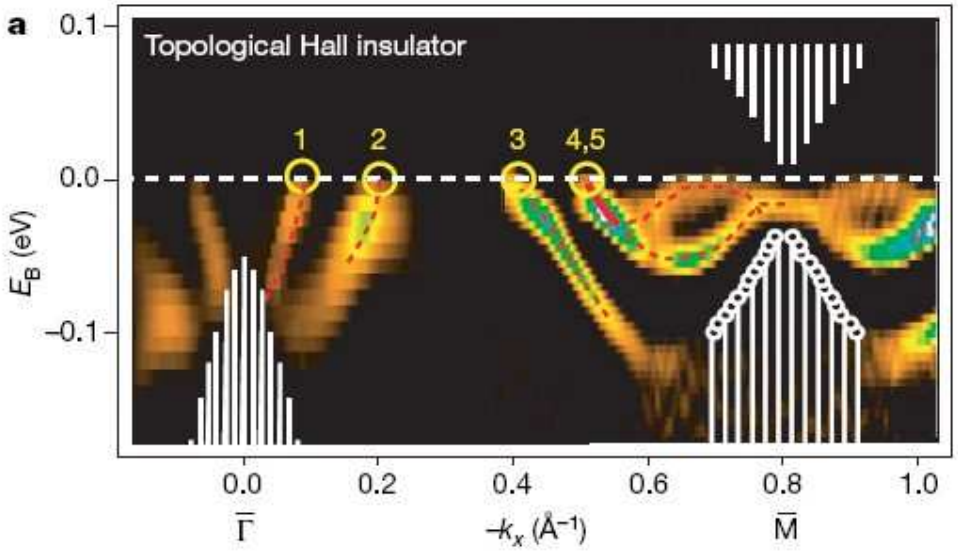

Fig. 19: [Reproduced from Ref. [20]] The surface bands along the $\bar{\Gamma}$-$\bar{M}$ path of the $Bi_{0.9}Sb_{0.1}$ (111) surface. The white shaded area is the projection of the bulk states measured by ARPES. The white dashed line is the Fermi level. The yellow circles indicate the Fermi level crossings of the surface bands, with the band near-k_x=0.5 Å^{-1} counted twice owing to double degeneracy. In total, there are five crossings indicated on the $\bar{\Gamma}$-$\bar{M}$ path, which shows that the surface is topologically non-trivial [20].

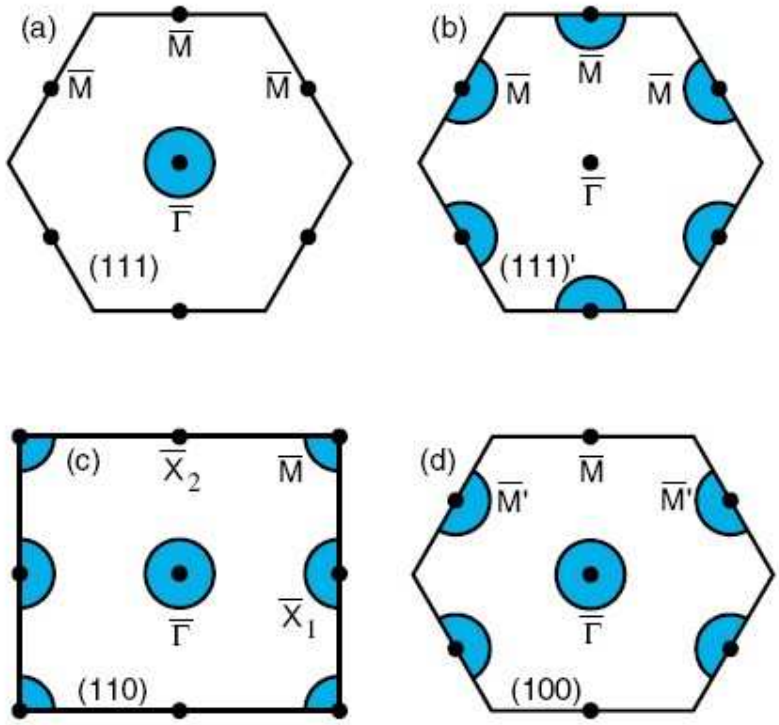

Fig. 20: [Reproduced from Ref. [23]] Illustrations of the Fermi surface enclosed time-reversal-invariant momenta in the First Brillouin zone for different $Bi_{1-x}Sb_x$ surfaces: (a) (111), (b) (111)′, (c) (110), and (d) (100). The (111)′ surface is a hypothetical surface cleaved in the middle of a bi-layer of $Bi_{1-x}Sb_x$ [23].

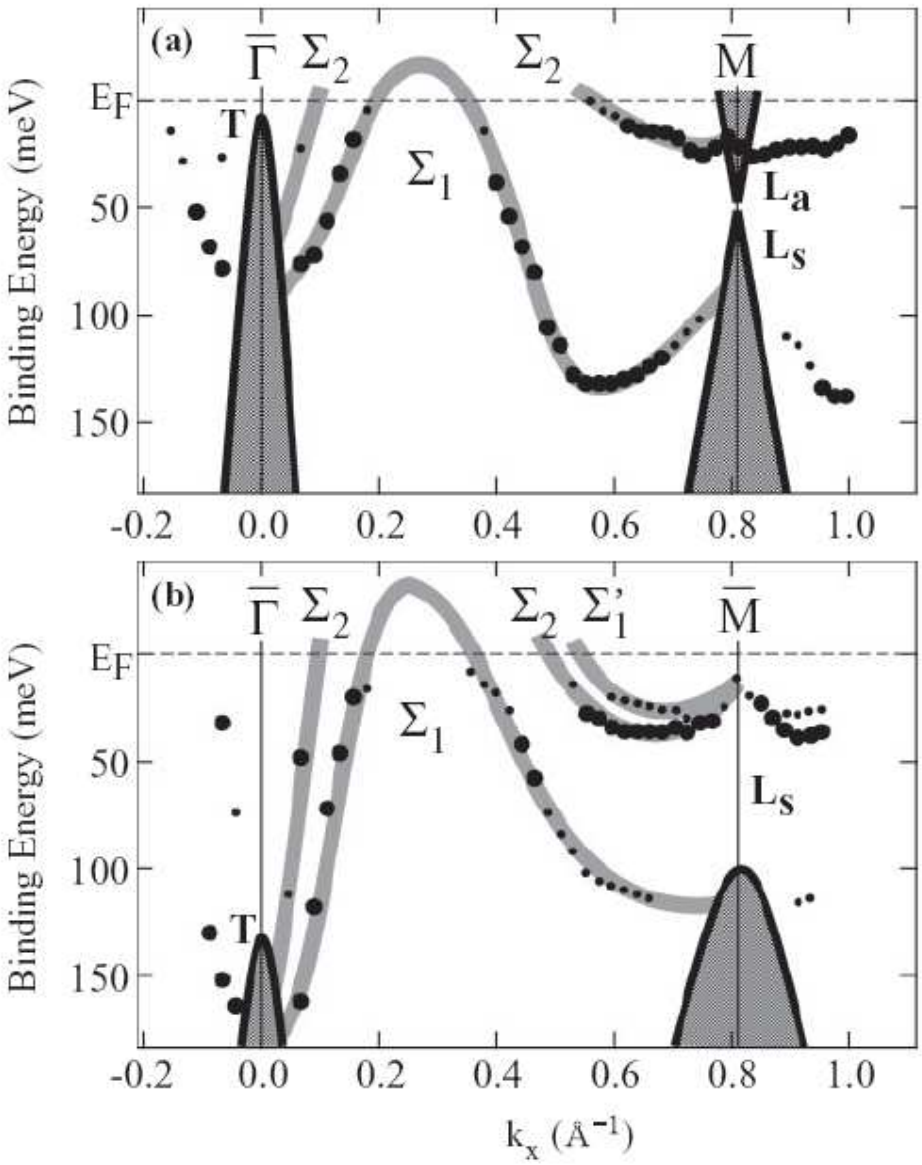

Fig. 21: [Reproduced from Ref. [24]] The band structures of $Bi_{1-x}Sb_x$ materials for Sb compositions (a) x = 0.04 and (b) x = 0.21, determined from ARPES spectra. The shaded regions denote the projected bulk states. The surface bands are labeled by Σ_1, Σ_1' and Σ_2, where the Σ_1 (Σ_1') has opposite spin orientations relative to the Σ_2 [24].

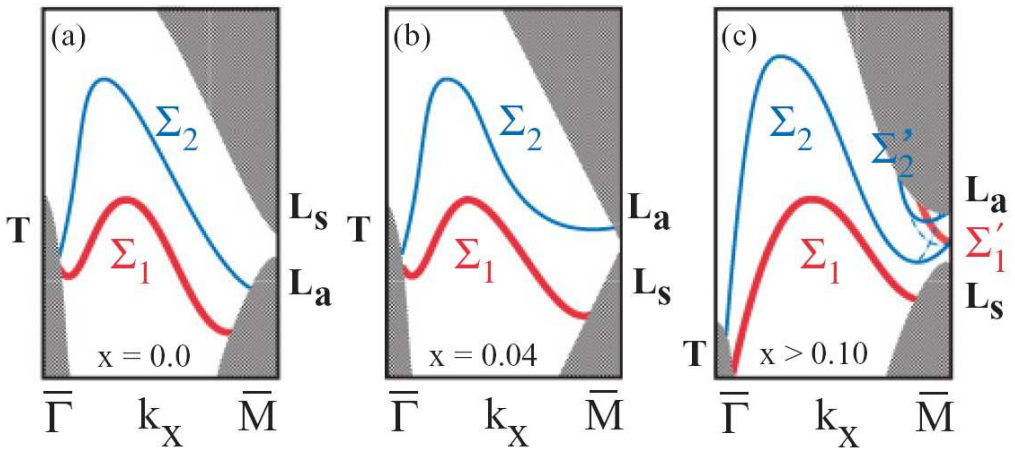

Fig. 22: [Reproduced from Ref. [24]] Schematics of how the topological insulator phase transition takes place in $Bi_{1-x}Sb_x$ (111) when the Sb composition increases from x=0. The shaded areas are the bulk state projections. The surface bands are labeled by Σ_1 and Σ_2, whose splitting bands are Σ_1' and Σ_2', separately, and Σ_1 (Σ_1') has opposite spin orientations with respect to Σ_2 (Σ_2'). (a) For x=0, the Σ_1 and Σ_2 bands are dispersed separately within the gap of the bulk, which merge into the bulk *T*-point valence band at the $\bar{\Gamma}$, and merge into the bulk *L*-point valence band at the $\bar{M}$ point. (b) When the Sb composition is increased to x=0.04, the bulk *L*-point direct band gap is zero, and the surface Σ_2 band at the $\bar{M}$ point merges into the bulk *L*-point conduction band, which makes the whole system have an odd number of Dirac cones at the surface state, and therefore, become topologically nontrivial. (c) When the Sb composition increased to x>0.10, the topologically nontrivial band Σ_1' (Σ_2') may split from the Σ_1 (Σ_2) band, and has the same spin-polarization as the Σ_1 (Σ_2) band, and this is shown by solid red and blue lines. The nontrivial bands Σ_2 and Σ_2' may hybridize with each other and form new bands at different Sb compositions, as shown by the dashed blue lines, which reproduce the experimental result of Fig. 19 [24].

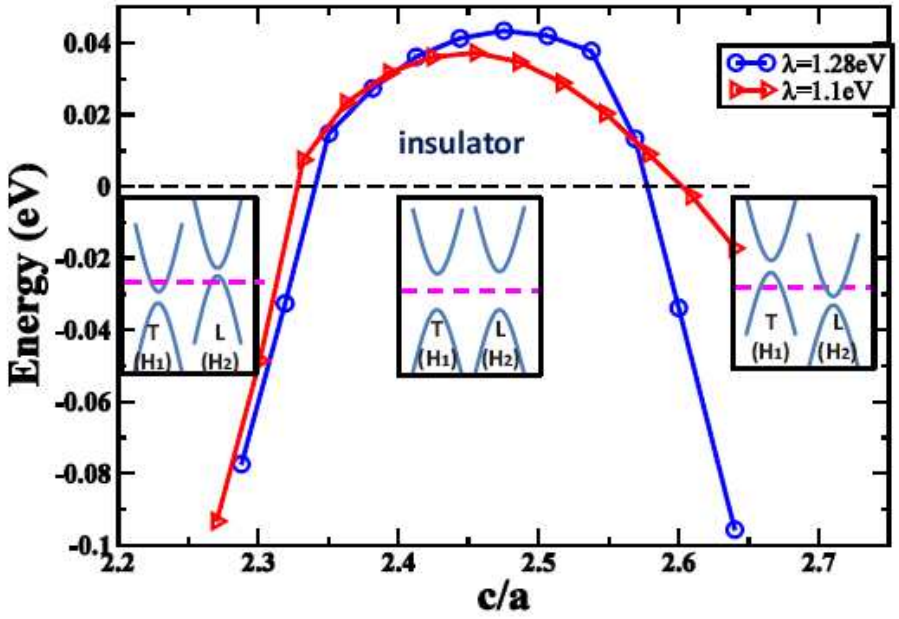

Fig. 23: [Reproduced from Ref. [25]] How to control the indirect band gap between the top of the valence band at the *T* point and the bottom of the electron band at the *L* point, as a function of the relative magnitude of the trigonal axis lattice parameter **c**/**a**, under cases of two different spin-orbit coupling strengths λ in $Bi_{1-x}Sb_x$ materials [25].

	Rhombohedral Cell		Hexagonal Cell	
	a (Å)	***c*** (Å)	***t*** (Å)	***α*** (°)
Bi	4.547	11.8616	4.7459	57° 14′
Sb	4.307	11.273	4.5066	57° 6′

Table 1: Crystalline Parameters of Bi and Sb. For a rhombohedral lattice, the unit cell is characterized by the length of the base vectors ***t***, and the angle ***α*** between two base vectors, and for a hexagonal lattice, the unit cell is characterized by the length of the base vectors ***a*** in the hexagonal plane, and the length ***c*** of the base vector normal to that hexagonal plane.

Reference:

1. L. Hicks and M. Dresselhaus, *Phys. Rev. B*, 1993, **47**, 12727-12731.
2. L. Hicks and M. Dresselhaus, *Phys. Rev. B*, 1993, **47**, 16631-16634.
3. Y.-M. Lin, S. Cronin, O. Rabin, J. Y. Ying and M. Dresselhaus, *Applied physics letters*, 2001, **79**, 677.
4. O. Rabin, Y.-M. Lin and M. S. Dresselhaus, *Applied physics letters*, 2001, **79**, 81.
5. Y.-M. Lin, O. Rabin, S. Cronin, J. Y. Ying and M. Dresselhaus, *Applied physics letters*, 2002, **81**, 2403-2405.
6. A. Nikolaeva, L. Konopko, T. Huber, P. Bodiul, I. Popov and E. Moloshnik, *Journal of Electronic Materials*, 2012, 1-4.
7. A. A. Nikolaeva, L. A. Konopko, T. E. Huber, P. P. Bodiul and I. A. Popov, *Journal of Solid State Chemistry*, 2012.
8. D. Morelli, D. Partin and J. Heremans, *Semiconductor Science and Technology*, 1999, **5**, S257.
9. R. C. Mallik and V. Damodara Das, *Solid state communications*, 2005, **134**, 211-216.
10. E. I. Rogacheva, D. y. S. Orlova, M. S. Dresselhaus and S. Tang, in *MRS Fall Meeting & Exhibit-2010, MRS Online Proceedings Library*, Cambridge Univ Press, 2011.
11. S. Tang and M. S. Dresselhaus, *Physical Review B*, 2012, **86**, 075436.
12. S. Tang and M. S. Dresselhaus, *Nano letters*, 2012, **12**, 2021-2026.
13. S. Tang and M. S. Dresselhaus, *Nanoscale*, 2012, **4**, 7786-7790.
14. B. Landschreiber, E. Güneş, G. Homm, C. Will, P. Tomeš, C. Rohner, A. Sesselmann, P. Klar, S. Paschen, E. Müller and S. Schlecht, *Journal of Elec Materi*, 2013, 1-6.
15. B. Landschreiber, E. Güneş, C. Rohner, G. Homm, C. Will, A. Sesselmann, P. Klar, E. Müller and S. Schlecht, in *AIP Conference Proceedings*, 2012, p. 303.
16. K. Lukas, G. Joshi, K. Modic, Z. Ren and C. Opeil, *Journal of Materials Science*, 2012, **47**, 5729-5734.
17. K. C. Lukas, H. Zhao, R. L. Stillwell, Z. Ren and C. P. Opeil, *MRS Online Proceedings Library*, 2012, **1456**.
18. S. B. Cronin, Y.-M. Lin, O. Rabin, M. R. Black, J. Y. Ying, M. S. Dresselhaus, P. L. Gai, J.-P. Minet and J.-P. Issi, *Nanotechnology*, 2002, **13**, 653.
19. A. Nikolaeva, P. Bodiul, L. Konopko and G. Para, in *Thermoelectrics, 2002. Proceedings ICT'02. Twenty-First International Conference on*, IEEE, 2002, pp. 272-275.
20. D. Hsieh, D. Qian, L. Wray, Y. Xia, Y. S. Hor, R. Cava and M. Z. Hasan, *Nature*, 2008, **452**, 970-974.
21. L. Fu and C. L. Kane, *Physical Review B*, 2007, **76**, 045302.
22. A. Nishide, A. A. Taskin, Y. Takeichi, T. Okuda, A. Kakizaki, T. Hirahara, K. Nakatsuji, F. Komori, Y. Ando and I. Matsuda, *Physical Review B*, 2010, **81**, 041309.
23. J. C. Teo, L. Fu and C. Kane, *Physical Review B*, 2008, **78**, 045426.
24. F. Nakamura, Y. Kousa, A. A. Taskin, Y. Takeichi, A. Nishide, A. Kakizaki, M. D'Angelo, P. Lefevre, F. Bertran and A. Taleb-Ibrahimi, *Physical Review B*, 2011, **84**, 235308.
25. H.-J. Zhang, C.-X. Liu, X.-L. Qi, X.-Y. Deng, X. Dai, S.-C. Zhang and Z. Fang, *Physical Review B*, 2009, **80**, 085307.
26. B. Poudel, Q. Hao, Y. Ma, Y. Lan, A. Minnich, B. Yu, X. Yan, D. Wang, A. Muto and D. Vashaee, *Science*, 2008, **320**, 634-638.
27. K. Biswas, J. He, I. D. Blum, C.-I. Wu, T. P. Hogan, D. N. Seidman, V. P. Dravid and M. G. Kanatzidis, *Nature (London)*, 2012, **489**, 414-418.
28. A. L. Jain, *Physical Review*, 1959, **114**, 1518.
29. K.-H. Hellwege, O. Madelung and M. Schultz, *Landolt-Bornstein Numerical Data and Functional Relationships in Science and Technology*, Springer-Verlag, Berlin, 1987.
30. W. Yim and A. Amith, *Solid-State Electronics*, 1972, **15**, 1141-1165.
31. N. Brandt, Y. G. Ponomarev and S. Chudinov, *Journal of Low Temperature Physics*, 1972, **8**, 369-420.
32. A. W. Smith, *Physical Review (Series I)*, 1911, **32**, 178.
33. H. Jones, *Proceedings of the Royal Society of London. Series A-Mathematical and Physical Sciences*, 1934, **147**, 396-417.
34. H. Jones, *Proceedings of the Royal Society of London. Series A, Mathematical and Physical Sciences*, 1936, **155**, 653-663.
35. H. Chu and Y.-H. Kao, *Physical Review B*, 1970, **1**, 2369.
36. E. Tichovolsky and J. Mavroides, *Solid State Communications*, 1969, **7**, 927-931.
37. T. Yazaki and Y. Abe, *Journal of the Physical Society of Japan*, 1968, **24**, 290-295.

38. L. R. Windmiller, *Phys. Rev.*, 1966, **149**, 472-484.
39. G. E. Smith, G. A. Baraff and J. M. Rowell, *Physical Review*, 1964, **135**, A1118-A1124.
40. A. Gerritsen and W. de Haas, *Physica*, 1940, **7**, 802-816.
41. A. Gerrttsen, W. de Haas and P. van der Star, *Physica*, 1942, **9**, 241-247.
42. G. Smith, *Phys. Rev. Lett.*, 1962, **9**, 487-489.
43. R. N. Brown, J. G. Mavroides and B. Lax, *Physical Review*, 1963, **129**, 2055-2061.
44. R. T. Isaacson and G. A. Williams, *Physical Review*, 1969, **185**, 682-688.
45. R. T. Isaacson and G. A. Williams, *Physical Review*, 1969, **177**, 738-746.
46. W. Datars and J. Vanderkooy, *IBM Journal of Research and Development*, 1964, **8**, 247-252.
47. R. J. Dinger and A. Lawson, *Physical Review B*, 1973, **7**, 5215.
48. S. J. Freedman and H. J. Juretschke, *Physical Review*, 1961, **124**, 1379-1386.
49. M. P. Vecchi and M. S. Dresselhaus, *Phys. Rev. B*, 1974, **10**, 771.
50. N. Brandt and Y. G. Ponomarev, *Soviet Journal of Experimental and Theoretical Physics*, 1969, **28**, 635.
51. N. Brandt and S. Chudinov, *Soviet Journal of Experimental and Theoretical Physics*, 1971, **32**, 815.
52. N. Brandt, S. Chudinov and V. Karavaev, *ZHUR EKSPER TEORET FIZIKI*, 1971, **61**, 689-704.
53. H. Krüger, R. Herrmann, B. Fellmuth and W. Kraak, *physica status solidi (b)*, 1979, **93**, 661-667.
54. E. Mendez, A. Misu and M. Dresselhaus, *Physical Review B*, 1981, **24**, 639.
55. H. Krüger, R. Herrmann and G. Oelgart, *physica status solidi (b)*, 2006, **72**, K91-K93.
56. V. Shubha, S. Dutta and T. Ramesh, *J. High temps high press*, 2008, **37**, 317.
57. S. Dutta, V. Shubha and T. Ramesh, *Physica B: Condensed Matter*, 2010, **405**, 1239-1243.
58. A. Ohmura, A. Yamamura, M. Einaga, F. Ishikawa, A. Nakayama, Y. Yamada and S. Nakano, in *Journal of Physics: Conference Series*, IOP Publishing, 2012, p. 022088.
59. E. Fenton and J.-P. Jan, DTIC Document, 1971.
60. E. Bogdanov, D. Komarkov and W. Kraak, *physica status solidi (b)*, 1990, **160**, K33-K36.
61. R. Pozhera and R. Tolutis, *Fiz. Tverd. Tela.*, 1981, **23**, 3366-3371.
62. L. S. Lerner, K. F. Cuff and L. R. Williams, *Reviews of Modern Physics*, 1968, **40**, 770.
63. B. Lenoir, M. Cassart, J.-P. Michenaud, H. Scherrer and S. Scherrer, *Journal of Physics and Chemistry of Solids*, 1996, **57**, 89-99.
64. E. I. Rogacheva, A. A. Drozdova, O. N. Nashchekina, M. S. Dresselhaus and G. Dresselhaus, *Applied Physics Letters*, 2009, **94**, 202111-202113.
65. W. Kraak, G. Oelgart, G. Schneider and R. Herrmann, *physica status solidi (b)*, 1978, **88**, 105-110.
66. B. Lenoir, A. Dauscher, M. Cassart, Y. I. Ravich and H. Scherrer, *J. Phys. Chem. Solids*, 1998, **59**, 129-134.
67. E. Rogacheva, A. Yakovleva, V. Pinegin and M. Dresselhaus, *J. Phys. Chem. Solids*, 2008, **69**, 580-584.
68. N. Brandt and E. Svistova, *Journal of Low Temperature Physics*, 1970, **2**, 1-35.
69. N. Brandt and S. Chudinov, *ZHUR EKSPER TEORET FIZIKI*, 1970, **59**, 1494-1508.
70. N. Brandt and S. Chudinov, *Journal of Low Temperature Physics*, 1972, **8**, 339-365.
71. B. Lax, J. G. Mavroides, H. J. Zeiger and R. J. Keyes, *Phys. Rev. Lett.*, 1960, **5**, 241.
72. M. Dresselhaus, *J. Phys. Chem. Sol*, 1971, **32**, 3–33.
73. P. Y. Yu and M. Cardona, *Fundamentals of semiconductors: physics and materials properties*, Springer Berlin etc, 1999.
74. J.-P. Issi, *Australian Journal of Physics*, 1979, **32**, 585-628.
75. E. E. Mendez, A. Misu and M. S. Dresselhaus, *Phys. Rev. B*, 1981, **24**, 639.
76. E. E. Mendez, Massachusetts Institute of Technology, 1979.
77. O. Rabin, Massachusettes Institute of Technology, 2004.
78. Y.-M. Lin, S. B. Cronin, O. Rabin, J. Y. Ying and M. S. Dresselhaus, *MRS Online Proceedings Library*, 2001, **691**.
79. S. Tang and M. Dresselhaus, *Physical Review B*, 2014, **89**, 045424.
80. A. Fedorenko, V. Kosevich and L. Palatnik, in *Akademia Nauk SSSR, Doklady*, 1967, pp. 69-71.
81. A. Adkhamov, *Izv. Akad. Nauk TadzhSSR., Otd. Fiz.-Mat. Geol-Khim. Nauk.*, 1978, 113-114.
82. V. D. Das and M. Jagadeesh, *Vacuum*, 1981, **31**, 75-77.
83. S. Takabe, H. Osono and S. Kaneda, *Thin solid films*, 1986, **145**, 171-184.
84. F. Völklein and U. Dillner, *physica status solidi (b)*, 1990, **162**, 147-153.

85. D. Partin, J. Heremans, D. Morelli, C. Thrush, C. Olk and T. Perry, *Physical Review B*, 1988, **38**, 3818.
86. S. Cho, A. DiVenere, G. K. Wong, J. B. Ketterson and J. R. Meyer, *Physical Review B*, 1999, **59**, 10691.
87. K. Novoselov, A. Geim, S. Morozov, D. Jiang, Y. Zhang, S. Dubonos, I. Grigorieva and A. Firsov, *Science*, 2004, **306**, 666.
88. K. S. Novoselov, A. K. Geim, S. V. Morozov, D. Jiang, M. I. Katsnelson, I. V. Grigorieva, S. V. Dubonos and A. A. Firsov, *Nature (London)*, 2005, **438**, 197-200.
89. Y. Zhang, Y.-W. Tan, H. L. Stormer and P. Kim, *Nature (London)*, 2005, **438**, 201-204.
90. J. Moore, *Nature Physics*, 2009, **5**, 378-380.
91. V. Gusynin, S. Sharapov and J. Carbotte, *Int. J. Mod Phys B*, 2007, **21**, 4611-4658.
92. I. Gierz, C. Riedl, U. Starke, C. R. Ast and K. Kern, *Nano Lett.*, 2008, **8**, 4603-4607.
93. W. Dang, H. Peng, H. Li, P. Wang and Z. Liu, *Nano Lett.*, 2010, **10**, 2870-2876.
94. J. Zabel, R. R. Nair, A. Ott, T. Georgiou, A. K. Geim, K. S. Novoselov and C. Casiraghi, *Nano Lett.*, 2012, **12**, 617-621.
95. C.-W. Zhang and S.-S. Yan, *The Journal of Physical Chemistry C*, 2012, **116**, 4163-4166.
96. A. H. C. Neto, F. Guinea, N. Peres, K. Novoselov and A. Geim, *Reviews of Modern Physics*, 2009, **81**, 109.
97. B. Buttner, C. X. Liu, G. Tkachov, E. G. Novik, C. Brune, H. Buhmann, E. M. Hankiewicz, P. Recher, B. Trauzettel, S. C. Zhang and L. W. Molenkamp, *Nat Phys*, 2011, **7**, 418-422.
98. T. Dey and S. Ghatak, *Pramana*, 1989, **32**, 161-166.
99. T. Dey, *Pramana*, 1990, **34**, 243-248.
100. J. P. Heremans, C. M. Thrush, D. T. Morelli and M.-C. Wu, *Physical Review Letters*, 2002, **88**, 216801.
101. J.-P. Issi and J. Mangez, *Physical Review B*, 1972, **6**, 4429.
102. J.-P. Issi and J. Boxus, *Cryogenics*, 1979, **19**, 517-519.
103. J. Boxus and J.-P. Issi, *Journal of Physics C: Solid State Physics*, 1977, **10**, L397.